Final Report for ONR project on Time-Modulated Metasurfaces

ONR grant No. N00014-19-1-2011

Principal Investigator: Prof. Andrea Alù

Photonics Initiative, Advanced Science Research Center, City University of New York

85 St. Nicholas Terrace, New York, NY 10031, USA
Tel. +1.512.496.4963, email: aalu@gc.cuny.edu

URL: http://alulab.org

In the following, we review the main achievements supported by the ONR grant No. N00014-19-1-2011 on Nonlinear Topological Metamaterials. The period of performance spanned across the time period from January 1, 2019 to December 31, 2021.

1. Executive Summary

During this three-year effort, we have made significant progress on the theoretical understanding, numerical modeling and experimental realization and characterization of nonlinear topological metamaterials, with a focus on nanophotonics, and encompassing topological phenomena in reciprocal space (in the band diagrams of periodic metamaterials), in real space and in synthetic space (in the space of parameters controlling a given system). Our results have been featured in several publications, including 39 journal papers, 1 book chapter, 51 conference abstracts and presentations, and several other seminars and tutorials. The high-profile results stemming from this research project have been published in high-profile journals, including in Science, Nature, Nature family journals and other high-impact, highly selective scientific journals. Our papers have been featured on various journal covers, selected as Editors' Picks, and featured in Press Releases and news coverages. Thanks to this research support, the PI and supported personnel (3 graduate students and 2 postdocs) have received several honors, awards and recognitions. One graduate student supported by this funding will complete his studies this summer and is considering various options for his future career in academia and industry. All these achievements are listed in the Appendix of this report. In the next sections, we describe and summarize a few highlights from the research carried out within this project. More details on the research achievements of this project may be found in the associated scientific publications, listed in the Appendix to this document.

REPORT DOCUMENTATION PAGE

1. REPORT DATE	2. REPORT TYPE	3. DATES COVERED	
		START DATE	END DATE
06/08/2022	Final	01/01/2019	12/31/2021

4. TITLE AND SUBTITLE

Nonlinear topological metamaterials

5a. CONTRACT NUMBER	5b. GRANT NUMBER	5c. PROGRAM ELEMENT NUMBER
	N00014-19-1-2011	
5d. PROJECT NUMBER	**5e. TASK NUMBER**	**5f. WORK UNIT NUMBER**

6. AUTHOR(S)

Alu, Andrea

7. PERFORMING ORGANIZATION NAME(S) AND ADDRESS(ES)	8. PERFORMING ORGANIZATION REPORT NUMBER
Research Foundation of the City University of New York on behalf of Advanced Science Research Center RFCUNY-Advanced Science Research Center 85 ST NICHOLAS TERRACE NEW YORK NY 10031-1246	final

9. SPONSORING/MONITORING AGENCY NAME(S) AND ADDRESS(ES)	10. SPONSOR/MONITOR'S ACRONYM(S)	11. SPONSOR/MONITOR'S REPORT NUMBER(S)
Office of Naval Research 875 N. Randolph Street, Suite 1425 Arlington, VA 22203-1995		

12. DISTRIBUTION/AVAILABILITY STATEMENT

Approved for Public Release; Distribution is Unlimited

13. SUPPLEMENTARY NOTES

14. ABSTRACT

During this three-year effort, we have made significant progress on the theoretical understanding, numerical modeling and experimental realization and characterization of nonlinear topological metamaterials, with a focus on nanophotonics, and encompassing topological phenomena in reciprocal space (in the band diagrams of periodic metamaterials), in real space and in synthetic space (in the space of parameters controlling a given system). Our results have been featured in several publications, including 39 journal papers, 1 book chapter, 51 conference abstracts and presentations, and several other seminars and tutorials. The high-profile results stemming from this research project have been published in high-profile journals, including in Science, Nature, Nature family journals and other high-impact, highly selective scientific journals. Our papers have been featured on various journal covers, selected as Editors' Picks, and featured in Press Releases and news coverages. Thanks to this research support, the PI and supported personnel (3 graduate students and 2 postdocs) have received several honors, awards and recognitions. One graduate student supported by this funding will complete his studies this summer and is considering various options for his future career in academia and industry. All these achievements are listed in the Appendix of this report. In the next sections, we describe and summarize a few highlights from the research carried out within this project. More details on the research achievements of this project may be found in the associated scientific publications, listed in the Appendix to this document.

15. SUBJECT TERMS				
16. SECURITY CLASSIFICATION OF:			17. LIMITATION OF ABSTRACT	18. NUMBER OF PAGES
a. REPORT	b. ABSTRACT	C. THIS PAGE		

19a. NAME OF RESPONSIBLE PERSON	19b. PHONE NUMBER *(Include area code)*
Andrea Alu	212-413-3260

Our research on nonlinear topological metamaterials across the three years span of this project can be categorized in three classes: (i) topological polaritonics in reciprocal space, which deals with periodic metasurfaces with nontrivial topological features in their band diagrams, featuring extreme light-matter interactions with large tunability; (ii) topological polaritonics in real space, dealing with topological charges confined in space and carried by complex field profiles; (iii) topological phenomena in parameter space, including exceptional points and PT-symmetry. While covering all the output from our project is beyond the scope of this report, we survey the breadth of these investigations in the following sections. The interested reader can find details and further examples in our published work.

2. Topological polaritonics in reciprocal space

Polaritons are quasi-particles stemming from collective resonant oscillations of photons coupled to material resonances. They have been explored in recent years to push the boundaries of light manipulation at the sub-wavelength scale, as they offer opportunities to go well beyond the limits of passive, linear, time-invariant materials. For instance, they can offer broadband, enhanced localized light-matter interactions and extreme light confinement. Among the most popular approaches, phonon polaritons have been widely explored in recent years. These are based on the strong coupling of light with lattice vibrations of certain materials, typically arising on the long-wavelength (LWIR) or mid-wavelength (MWIR) infrared regimes. Recently, it has been discovered that phonon polariton resonances can be sufficiently strong to endow the underlying materials with a ***hyperbolic response***, as shown in various polar van der Waals (vdW) nanomaterials [1-6]. While most of these naturally occurring ***hyperbolic polaritons*** propagate out of plane because of the lattice resonance orientation in relation with the material growth axis, it has recently been shown that in-plane hyperbolic phonon polaritons can arise in α-phase molybdenum trioxide (α-MoO3) flakes. Within their Reststrahlen band (RB) from 818 cm^{-1} to 974 cm^{-1}, the real part of permittivity of α-MoO3 is negative along the [100] direction, but positive along the [001] direction. Such extreme anisotropy allows in-plane low-loss hyperbolic PhP propagation [6-8].

In a different context, our group has introduced and explored the concept of hyperbolic metasurfaces, showing how engineered nanoscale patterns over a surface can enable extreme anisotropy and ad-hoc in-plane light propagation with hyperbolic dispersion [9-11]. In particular, we have shown how these surfaces combine the unusual features of hyperbolic metamaterials, such as ***broadband enhancement of local density of states***, ***canalization***, ***sub-diffraction imaging*** and ***negative refraction***, with the advantage of supporting these exotic phenomena over a surface, not in the bulk, hence with more resilience to loss and easier accessibility. Hyerpbolic metasurfaces have been demonstrated over several material platforms, from silver gratings [12-13], nanostructured van der Waals materials [14-15], graphene nanoribbons [9] and black

phosphorus [10]. For instance, in the case of densely packed graphene nanoribbons, as in the inset of Fig. 1a, where each graphene strip has width *W* and an air gap *G* separating neighboring strips, if the periodicity is deeply subwavelength, the metasurface response can be homogenized with the effective surface conductivity tensor [11]

$$\bar{\bar{\sigma}} = \begin{bmatrix} \sigma_{\alpha\alpha} & 0 \\ 0 & \sigma_{\beta\beta} \end{bmatrix} \approx \begin{bmatrix} \frac{W}{P}\sigma_G & 0 \\ 0 & \frac{W\sigma_G\sigma_C}{P\sigma_c + W\sigma_G} \end{bmatrix}. \quad (1)$$

Here, $\sigma_C = -\frac{2i\omega\varepsilon_0 P}{\pi}\ln\left[\frac{1}{\sin(\pi G/2P)}\right]\sigma_C = -\frac{2i\omega\varepsilon_0 P}{\pi}\ln\left[\frac{1}{\sin(\pi G/2P)}\right]$ is the effective strip conductivity taking into account near-field coupling and nonlocality, σ_G is the pristine graphene conductivity, ω is the radial frequency, and ε_0 is the free-space permittivity. α and β are defined perpendicular and parallel to the ribbon directions, respectively. In the hyperbolic regime, the metasurface acts as a metal for one transverse field polarization ($\mathrm{Im}[\sigma_{\alpha\alpha}]>0$) and as a dielectric for the other one ($\mathrm{Im}[\sigma_{\beta\beta}]<0$). The field distributions (E_z) and dispersion bands, obtained as the Fourier spectrum of the field excited by a broadband *z*-oriented dipole simulated using a full-wave commercial software, are shown in Figs. 1b-c, which indeed demonstrates collimated field profiles. We have used these surfaces for a variety of exciting nanophotonic opportunities, including our recent work on valleytronics [13], in which we showed enhanced exciton-polariton emission that can be also made directional by the proper design of hyperbolic metasurfaces.

During this project, we were able to push these concepts forward by adding twisting and rotational symmetry breaking into the picture [16]. In particular, we showed that a twisted stack of hyperbolic metasurfaces can extend the concept of twistronics recently introduced in electronic systems [17] to photons, enabling an extreme control of the polariton dispersion, analogous to moiré physics but for nanoscale light. As shown in Fig. 1d-g, the response of these twisted polaritonic metasurfaces can be reconfigured from hyperbolic to elliptical topologies over a broad range of wavelengths by simply changing the rotation angle between them, offering broadband reconfigurability of the enhanced local density of states, and tracking of the ***photonic magic angle*** between the two twisted surfaces at which the topological transition occurs with frequency [16]. At the same time, the extreme anisotropy of these artificial metastructures, at the basis of their hyperbolic response, is fundamentally limited by their granularity, inducing strong nonlocality [9-11], which fundamentally hinders the practical verification of these concepts in terms of a limit to the local density of states and maximum wave number for which hyperbolic phenomena can occur.

By exploiting the natural hyperbolicity of α-MoO3, instead of hyperbolic metasurfaces, we have been able to observe these phenomena using near-field scanning optical

microscopy [18], as shown in Fig. 2, over twisted bilayers. At fixed frequency, we observe a topological transition from closed to open contours as a function of the twist angle, and we can scan the frequency to tune the occurrence of this topological transition, offering a way to achieve largely reconfigurable, low-loss, diffraction-free nanoscale light manipulation and extreme dispersion engineering [18].

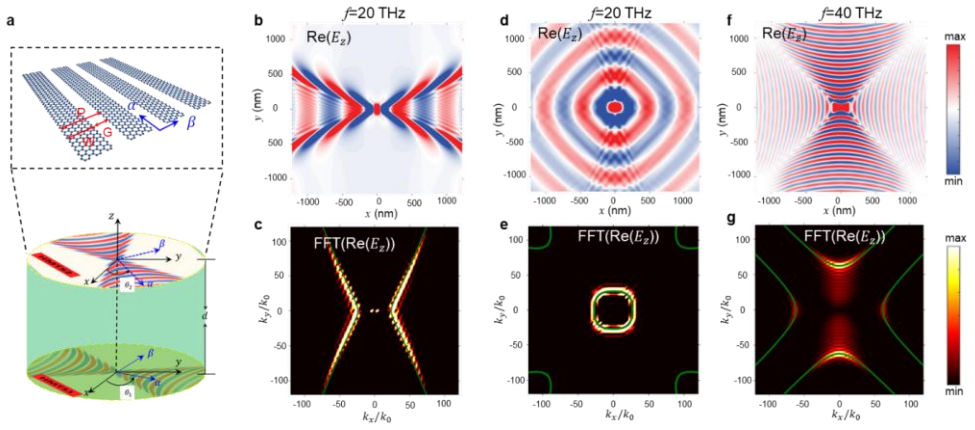

Figure 1. Geometry, field distributions and dispersion of hyperbolic and moiré metasurfaces. |(a) Geometry of moiré hyperbolic metastructures, composed of two coupled hyperbolic metasurfaces with different rotation angles θ_1 and θ_2 with respect to $\boldsymbol{x}$. Their prime characteristic directions are denoted as α and β. Two metasurfaces are separated by a dielectric spacer and thickness d. (b). E_z distribution for an individual hyperbolic metasurface in vacuum and (c) its dispersion at frequency f=20THz. (d) E_z distribution for the moiré metasurface and (e) its dispersion at frequency f=20THz. (f) E_z distribution for the moiré metasurface and (g) its dispersion at f=40THz. The green curve in c, e and g are the numerically calculated dispersion. Metasurfaces in (b) and (c) are composed by graphene ribbons (P=50nm, W=30nm, Fermi level = 0.4eV and $\tau = 0.5$ps). The moiré metasurfaces in (d) and (e) is composed of the same graphene ribbons with $\theta_1 = 0$, $\theta_2 = 90°$ and $d = 10$nm. (From [16])

This result offers an interesting outlook into the unique opportunities that polaritonics combined with metamaterial concepts offer in the context of extreme light manipulation at the nanoscale, enabling unique opportunities for nonlinear light-matter interactions over broad bandwidths. This project has allowed us to discover that the role that lattice symmetries play in these natural and engineered materials, the angles that the lattice resonances form with the interfaces play a major role in determining the unusual responses, and the phenomena unveiled in [16,18] are just one example of a totally new research direction for nanophotonics, driven by topological concepts. By introducing lower-symmetry materials, we have indeed been able to show even more remarkable manipulation of nanoscale light based on topological polaritons. For instance, using calcite (calcium carbonate), we have been able to leverage its extreme anisotropy through

the angle that the optical axis (OA) orientation can feature with respect to the material interface with air, leading to ghost hyperbolic polaritons (g-HPs) bound to the interface but with tilted phase fronts entering the bulk [19].

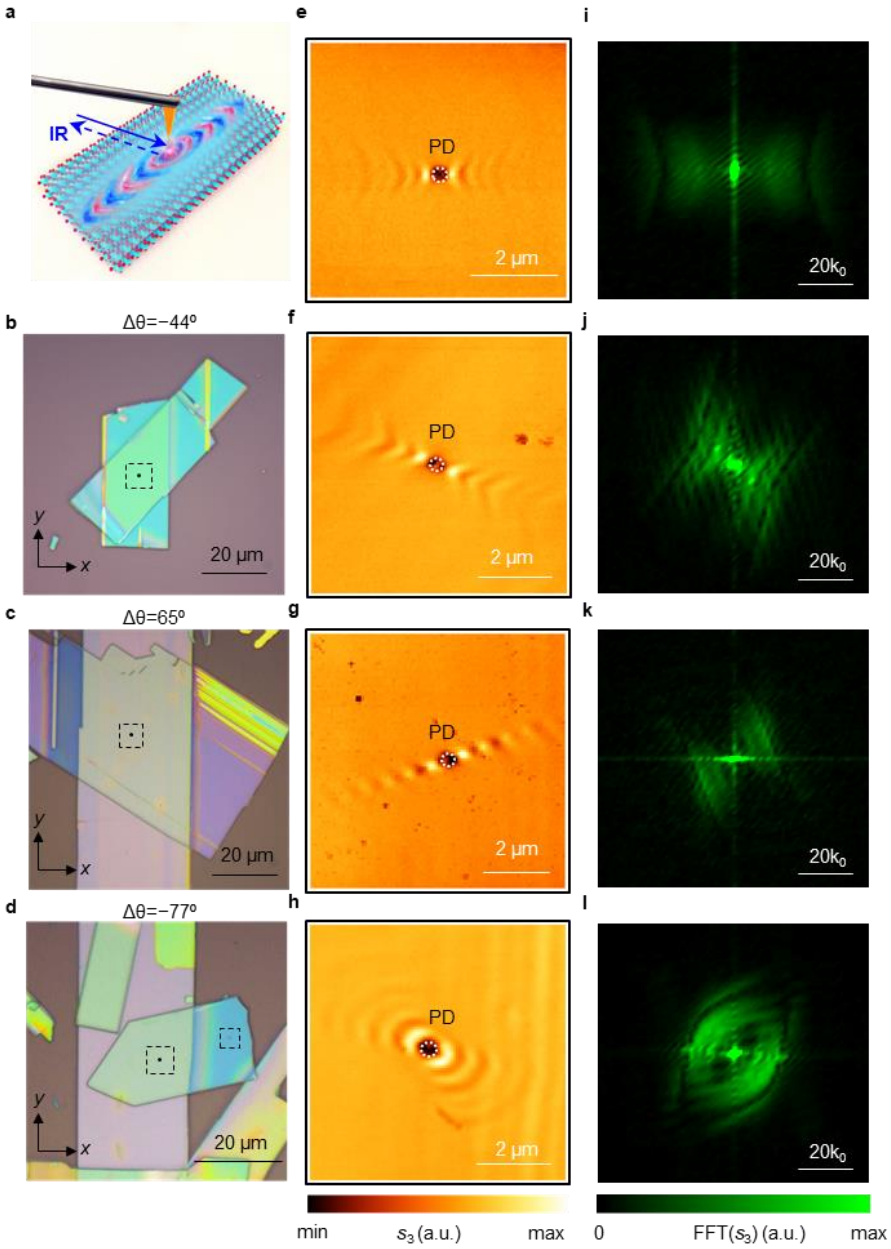

Figure 2. Experimental observation of reconfigurable topological transitions of phonon polaritons. a, Schematics of s-SNOM nanoimaging of phonon polaritons on α-MoO_3 twisted bilayer. Upon infrared light illumination, the metallic tip launches the polaritons in the sample, which are then scattered into free space for collection. **b-d**, Optical images of α-MoO_3 bilayer samples for twist angle Δθ=-44˚ (d_1=d_2=128 nm), Δθ=65˚ (d_1=120 nm, d_2=235 nm) and Δθ=-77˚ (d_1=125 nm, d_2=210 nm). **e-h,**

Experimentally measured near-field distribution near a point defect (PD) denoted by white dashed circles: **e** is measured near the PD in the top layer of sample with Δθ=-77˚ (the top dashed square areas in panel **d**); **f**, **g**, and **h** are measured in the α-MoO_3 bilayer in the dashed square areas of panel **b**, **c**, and **d**. The PD diameter is around 200 nm. **i-l,** Dispersion curves obtained by Fourier transform of the measured near-field signal in **e**, **f**, **g** and **h**. All measurements refer to ω=903.8 cm^{-1}. The black dots in panel **b**, **c**, and **d** represent the PD. (From [**Error! Reference source not found.**])

Further lowering the symmetry, we have shown that monoclinic crystals like β-Ga_2O_3 have been recently shown to support shear hyperbolic polaritons, in which non-orthogonal phonon resonances sustain hyperbolic propagation with asymmetric loss profiles and an OA rotating as a function of frequency [20]. The growing family of polaritonic materials has been opening truly unique opportunities for light-matter nanoscale routing, transport and manipulation.

Even more recently, in unpublished work, we have been able to show remarkable control over topological polaritons, demonstrating that natural anisotropic crystals can support a new regime for polariton propagation inherently leaky in nature, which is at the same time bound to the interface with air and hybridized with refractive bulk modes. This class of polaritons features a new form of iso-frequency dispersion contours (IFCs) with a peculiar lenticular shape, forming a cusp or a wedge at a high-symmetry point in momentum space. Interestingly, despite featuring IFCs with a closed topology, i.e., limited to a finite region in momentum space, these leaky polaritons (LPs) support long-distance highly directional propagation along the material interface, which naturally couples to radiation accessible within the bulk of the material.

To reveal their features, we study the exemplary case of polaritons at the interface between air and calcite. Calcite is a uniaxial polar crystal whose OA can be slanted with respect to the interface by an angle θ [Fig. 3a]. Polaritons at the calcite-air interface have been recently explored in the upper Reststrahlen band [19], for which the principal permittivity components $\epsilon_{\parallel} > 0$ and $\epsilon_{\perp} < 0$, parallel and perpendicular to the OA, respectively, are associated with a type-II hyperbolic dispersion of their phonon polaritons. When $\theta \neq 0°$, the broken symmetry between the phonons and the interface tilts their wave vectors with respect to the interface, leading to the emergence of g-HPs, as shown in Fig. 1a for $\omega = 1470\ \mathrm{cm}^{-1}$, which are bound to the interface but feature a tilt of their phase fronts entering the calcite bulk. The Fourier transform (FT) of the in-plane fields (Fig. 3b) is associated with a hyperbolic IFC, shown in Fig. 3c. In contrast, the lower Reststrahlen band, for which $\epsilon_{\parallel} < 0$ and $\epsilon_{\perp} > 0$, supports type-I hyperbolic phonon polaritons in the bulk. This frequency range, as well as the neighboring ε-near-zero transparent regime where $\epsilon_{\perp} > 0$ and $0 < \epsilon_{\parallel} < \epsilon_{air}$, both support the emergence of

LPs at the interface with air. When excited by a localized emitter in the hyperbolic regime at $\omega = 887\text{cm}^{-1}$ (Fig. 3a), the LP field distribution is remarkably directional in the interface plane (Fig. 3d), showing four emission lobes. The corresponding FT, however, is associated with an IFC with a peculiar lenticular shape (Fig. 3e), with a closed topology despite the directionality of emission.

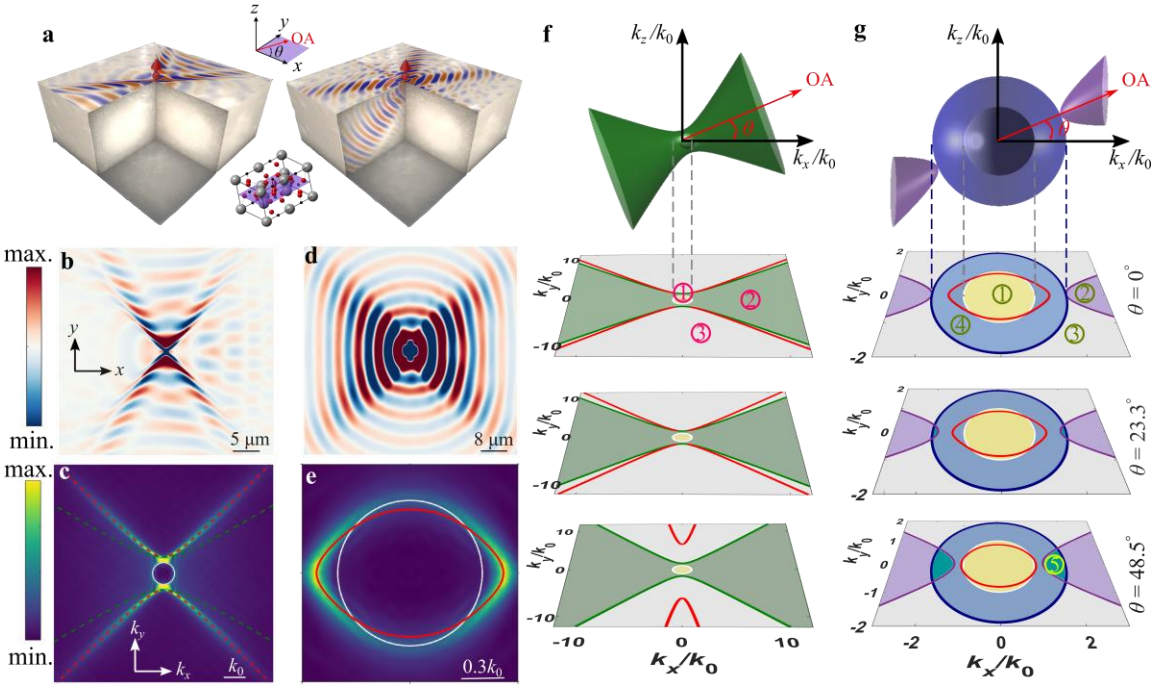

Figure 3. Ghost and leaky polaritons (LPs). (a) Schematic of the excitation of ghost hyperbolic polaritons (g-HPs) in the left panel and LPs in the right panel, emerging at the interface between calcite and air, and supporting directional waves that propagate on the surface and in the bulk of calcite. (b, d) Real space distribution of simulated field $\Re(E_z)$ on the surface of calcite and (c, e) the corresponding FT in *k*-space, respectively. (f) 3D isofrequency contours (IFCs) for type-II hyperbolic regime at frequency ($\omega = 1470\text{cm}^{-1}$) supporting g-HPs and (g) 3D IFCs for type-I hyperbolic regime at frequency ($\omega = 887\text{cm}^{-1}$) supporting LPs, and their dependence of the in-plane momentum dispersion on the slanted optical axis of calcite. The green solid lines in f (green dashed lines in c) represent the light cones of extraordinary wave in type-II hyperbolic regime, blue and purple solid lines in g represent the light cones of ordinary wave and extraordinary wave in the type-I hyperbolic regime. The red solid lines in f (red dashed lines in c) are the dispersion of g-HPs obtained from Eq. (1), and the red solid lines in e, g are the dispersion of LPs obtained from Eq. (2). The white sphere depicts the IFC of free space, and white circle is the FSLC.

These exotic dispersion features can be analyzed and explained by solving source-free Maxwell's equations at the calcite-air interface, for the moment neglecting material absorption. The polariton dispersion is computed by enforcing the continuity of the tangential fields at the interface: assuming that the in-plane wavenumbers in the *x*/*y* directions $k_{x,y}$ are real-valued, we obtain

$$\det\left(\widehat{\mathrm{D}}\left(k_x, k_y\right)\right) = 0, \tag{1}$$

where $\widehat{\mathrm{D}}$ is a 4×4 matrix. The in-plane dispersion of g-HPs in the type-II hyperbolic regime at $\omega = 1470\ \mathrm{cm}^{-1}$ is shown as a red dashed curve in Fig. 3c, in agreement with the FT of the near-fields. In this regime, calcite only supports the propagation of extraordinary waves in the bulk, and their IFC is a hyperboloid aligned with the OA (generally oriented at an angle θ with respect to the interface, as shown in Fig. 3f). Around the origin, we also show the spherical IFC of free-space radiation modes. When projected onto the interface plane, three different regions emerge for the in-plane momentum: (1) the free-space light cone (FSLC) (white circle), (2) the light cone of extraordinary waves in calcite (green hyperbolae), and (3) the remainder of the in-plane *k*-space (gray) where no bulk modes are supported at either side of the interface. Surface hyperbolic polaritons (s-HPs) ($\theta = 0°$) and g-HPs ($\theta \neq 0°$) guided at the interface and with real in-plane wave numbers are supported in region (3), with their dispersion depicted by red lines in Fig. 3f, bound to the interface, carrying power along it and evanescently decaying away from it.

In contrast, LPs result from the hybridization of surface-bound modes with propagating bulk waves. They naturally emerge in the type-I hyperbolic regime, e.g., at $\omega = 887\ \mathrm{cm}^{-1}$ for calcite, in which bulk propagation is now associated with ordinary waves with isotropic dispersion in *k*-space, described by the outer sphere in Fig. 3g (top panel), as well as extraordinary waves with hyperbolic dispersion, described by the two purple hyperboloids with major axis parallel to the OA. The projected dispersions onto the k_x, k_y (interface) plane show a more complex geometry, with four distinct regions: regions (1-3) (R1-R3) resemble the ones in the type-II hyperbolic regime. In addition, R(4) outside the FSLC (blue ring) supports the propagation of ordinary bulk waves. Thus, while the extraordinary interface mode with in-plane momentum in R(1) can radiatively leak to both sides of the interface, in R(4) the interface modes are confined on the air side but leak into a refractive ordinary wave in the calcite bulk. As we tilt the OA with respect to the interface, $\theta \neq 0^{\circ}$ (bottom panels of Fig. 3f) a new region, R(5), appears due to the skewed hyperboloid projection overlapping with R(4), thus supporting radiation leakage into ordinary and extraordinary waves.

The in-plane momentum diagram in Fig. 3g implies that the interface modes can become compatible with radiation towards both sides of the interface [R(1)] or into calcite [R(4)],

hence we cannot generally expect guided modes with real-valued (k_x, k_y), even in the limit of negligible material dissipation. When searching for polariton modes at the air-calcite interface in this regime, we need to look for complex-valued wavenumbers satisfying Eq. (1) in the form $q = q_\mathrm{r} + \mathrm{i}q_\mathrm{i}$, for each real-valued polar angle ϕ in the k_x-k_y plane. As a result, Eq. (1) is split into two real-valued secular equations

$$\Re\left[\det\left(\widehat{\mathrm{D}}(q_r, q_i, \phi)\right)\right] = 0; \Im[\det\left(\widehat{\mathrm{D}}(q_r, q_i, \phi)\right)] = 0. \quad (2)$$

Working in the complex q plane, the choice of appropriate branch cuts and the sign of complex wave vectors becomes crucial to identify physical solutions. The resulting IFCs at $\omega = 887\mathrm{cm}^{-1}$ are shown as red lines in Fig. 3g for different values of θ. Interestingly, we observe the emergence of LPs, supported in R(1), R(4) of the in-plane k-space, with a peculiar lenticular dispersion featuring a closed topology, consistent with the numerical prediction in Fig. 3e. As we increase the angle θ between the OA and the interface, the extraordinary wave hyperboloids tilt, and hence their projections in the k_x- k_y plane move towards the center, forming R(5) and pushing the LP dispersion towards the origin in the k_x direction, until the critical angle $\theta_\mathrm{c} = \arctan\left(\sqrt{-\frac{\epsilon_\perp}{\epsilon_\parallel}}\right)$ at which the projected hyperbolic contours enter the FSLC, R(4) is split into two isolated regions separated by hyperbolic contours R(5), and hence LPs cannot be supported any longer.

The complex solutions of Eqs. (2) shown in Fig. 3e,g constitute the LP spectrum, which effectively hybridizes bulk ordinary waves in calcite with confined extraordinary surface modes, leading to a new form of polariton. Its hybrid features strongly depend on the in-plane momentum: for (k_x, k_y) parallel or adjacent to the direction of the OA, LPs display surface polariton ($\theta = 0^\circ$) or g-HP like ($\theta \neq 0^\circ$) features, with power flow nearly parallel to the interface and smaller radiation leakage, implying four lobes of highly directional emission into the bulk. When the in-plane wave vector rotates away from the OA, the LPs are more strongly coupled to the bulk ordinary wave with skewed wavefronts, hence their radiation leakage is larger and q_i increases outside the FSLC. The high-symmetry points $k_y = 0$ $(\phi = 0)$ and $k_x = 0$ $(\phi = \pi/2)$ are particularly interesting, as they correspond to the two extremes of the LPs hybrid nature: at $k_y = 0$ the LP is purely bound to the interface, while at $k_x = 0$ it is purely refractive and coupled to the ordinary bulk mode. At these two extremes, the imaginary part of the wavevector q_i notably vanishes. LPs can emerge also in the transparent regime, for example around $\omega = 890\ \mathrm{cm}^{-1}$. In this scenario, the IFCs follow a similar lenticular dispersion, but they are discontinuous when the direction of the wave vector comes close to the OA, because their dispersion intersects the extraordinary wave light line, which is now elliptical in shape.

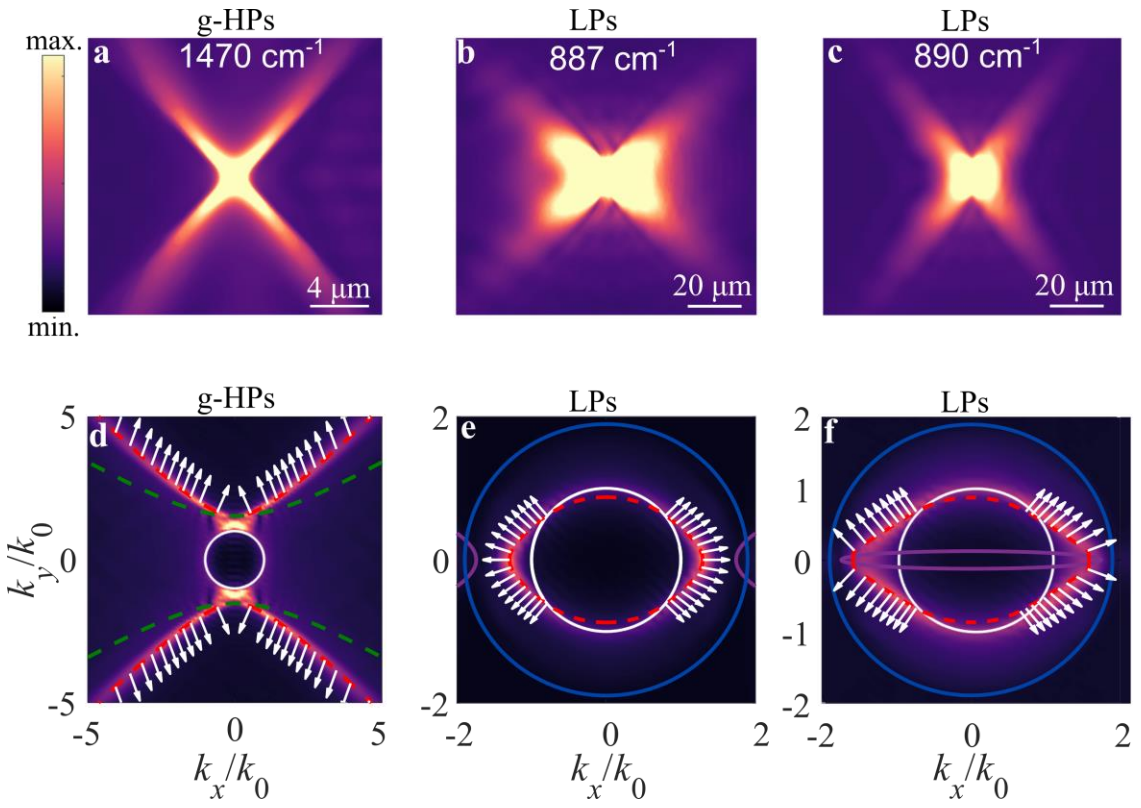

Figure 4. Directional propagation of LPs. **a-c**. Electric field amplitudes of polaritons in real space showing highly-directional propagation at frequency: **a**. $\omega = 1470\text{cm}^{-1}$, corresponding to g-HPs in the type-II hyperbolic regime; **b**. $\omega = 887\text{cm}^{-1}$, corresponding to LPs in type-I hyperbolic regime; **c**. $\omega = 890\text{cm}^{-1}$, corresponding to LPs in the transparent regime. In all cases $\theta = 23.3^{\circ}$. **d-f**. Corresponding in-plane dispersion (red curves) overlaid with Fourier spectra of the E_z fields from numerical simulations and normalized Poynting vectors (white arrows) of: **d**. g-HPs at frequency $\omega = 1470\text{cm}^{-1}$ calculated above the interface (in the air) and based on Eq. (1); **e**. LPs at frequency $\omega = 887\text{cm}^{-1}$; **f**. LPs at frequency $\omega = 890\text{cm}^{-1}$. Both e and f are calculated from Eqs. (2). All lines in d-f correspond to the same quantities as lines in Fig. 3.

As shown in Fig. 3a,d, LPs support peculiar directional features in the interface plane, despite being associated with closed contours. In order to explain this unexpected property of the lenticular dispersion, we analyze fields and Poynting vectors of LPs on the calcite interface plane for $\theta = 23.3^{\circ}$ in Fig. 4. In particular, we compare the magnitude of the electric field distribution of g-HPs (Fig. 4a) and LPs (Fig. 4b,c) in real space, and overlay the FT from their E_z fields with their in-plane dispersion obtained from Eq. (1) (Fig. 4d) and Eqs. (2) (Fig. 4e,f), considering realistic calcite loss. The emission directionality is associated with the Poynting vector direction for all in-plane

momenta, which is normal or nearly normal to the IFCs for surface polaritons. As shown in Fig. 4d, the Poynting vectors of g-HPs for each hyperbolic branch are mostly aligned to each other, due to the open topology of their dispersion, leading to highly directional propagation in real space. LPs, due to their peculiar lenticular dispersion, also feature power flows that are uncommonly parallel to each other in the same quadrant, exhibiting directional propagation in real space (Fig. 4b,c). This is surprising since the in-plane dispersion as shown in Fig. 4e,f has a closed or nearly closed topology for $\omega = 887\text{cm}^{-1}$ and $\omega = 890\text{cm}^{-1}$, corresponding to the type-I hyperbolic and transparent regimes, respectively. The brighter spectra outside the FSLC of the FT in Fig. 4e, f indicate the power flow in the plane is mainly associated with polaritons outside the FSLC, which indeed have Poynting vectors (white color in Fig. 4e,f) well aligned across the dispersion curve, far more than they would be with a conventional circular or elliptic dispersion. This directionality is fostered by the fact that the LP propagation length is almost constant along the IFC, despite the increasing radiation leakage for increasing $|\phi|$. This effect arises because the effective material loss of the hybridized mode simultaneously decreases for increasing $|\phi|$, peculiarly leading to enhanced directionality.

To experimentally observe LPs, during our project we performed both polariton spectroscopy and real space near-field imaging microscopy. First, we probed the LP dispersion in the frequency domain using Otto-type prism coupling for a calcite-air interface with OA slanted by $\theta = 23.3°$. We placed a prism made of dielectric Thallium Bromoiodide (KRS5) above the air-calcite interface with a fixed air gap $\text{d}_{\text{gap}} = 4\ \mu\text{m}$, and acquired reflectance spectra at the prism back-surface for several azimuthal angles ϕ between the incidence plane and the OA, see Fig. 5a. By fixing the incidence angle β, we select a specific value of in-plane momentum $k_{\parallel}$ of the excited evanescent waves. The resulting reflectance spectra for $\beta = 27°$, corresponding to $\frac{q_r}{k_0} = 1.075$ at $\omega = 887$ cm^{-1}, are shown in Fig. 5b. We observe a high-quality polariton resonance at $\phi = 0°$ (OA parallel to the incidence plane), which blue-shifts and quickly broadens as we rotate the sample in either direction about its surface normal. The experimental data are in good agreement with transfer matrix simulations shown in Fig. 5c. In order to map the in-plane dispersion of LPs, we acquired the azimuthal dependence for several incidence angles, and extracted the resonance positions, as well as their quality (Q)-factors. The retrieved resonance frequency map shown in Fig. 5d, in excellent agreement with the simulated data in Fig. 5e, displays the peculiar lenticular LP dispersion. This is confirmed in the retrieved IFCs from these data (see Methods), shown in Fig. 5f, which provide direct experimental proof of the lenticular in-plane dispersion of LPs.

The experimental and simulated Q-factors of LPs in calcite are shown in Fig. 5g and h, respectively. We retrieved Q-factor values along the IFCs at multiple frequencies, as shown in Fig. 5i. Remarkably, we have been able to observe very large Q-factors,

exceeding 300, at $\phi = 0°$ and Q ~ 150 at $|\phi| = 20°$, demonstrating a long life time for LPs, despite their leaky nature, a consequence of the low damping of the associated optical phonon polarized in the OA direction, leading to unprecedented directional radiation leakage. These are ideal features for opportunities in nonlinear nanophotonics, and integrated nanophotonic circuits.

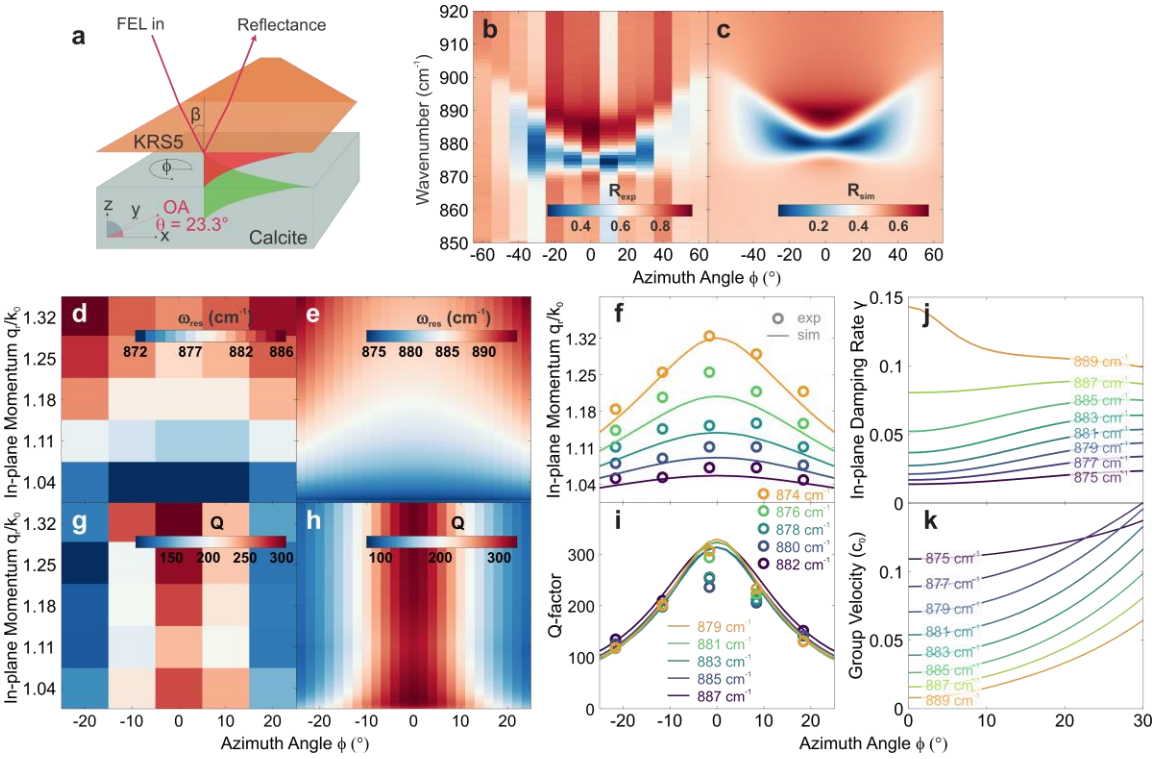

Figure 5. Otto-type prism coupling measurement for the experimental observation of LPs. a. Otto-type prism coupling configuration. **b.** Azimuthal dispersion extracted from experimental data and **c.** transfer matrix simulations for calcite (100), with optical axis tilted by $\theta = 23.3^{\circ}$ with respect to the interface (as displayed in a). These simulations were performed by taking into account the presence of a KRS5 prism when setting up the material system, and calculating for each configuration the corresponding reflectance spectrum. The in-plane momentum is fixed at $\frac{q}{k_0} = 1.07$. **d.** Experimental and **e.** simulated polariton resonance frequency map. The polariton resonance frequencies in the simulated maps are derived from the imaginary part of the reflection coefficients for *p*-polarized light Im(r_{pp}). **f.** Simulated (lines) and experimental (circles) IFCs at multiple frequencies, demonstrating the lenticular dispersion of LPs. **g.** Experimental and **h.** simulated LP Q-factors as a function of in-plane momentum. **i.** Simulated (lines) and experimental (circles) LP Q-factors along the IFCs at multiple frequencies. **j.** Calculated in-plane damping rate γ and **k.** group velocities v_g at multiple frequencies, demonstrating how the decreasing Q-factor for increasing $|\phi|$ is compensated by increased v_g for low net propagation losses, ultimately responsible for the directional propagation of LPs.

Strikingly, the Q-factors rapidly decrease for increasing $|\phi|$, for all momenta (Fig. 5h), and at all frequencies (Fig. 5i). Hence, the LPs experience a steep increase in optical loss as the polarization plane is rotated away from the OA. At first sight, this observation appears to contradict the theoretical prediction in Fig. 4, where nearly constant propagation loss along the IFC promotes the directional propagation features. In order to resolve this discrepancy, we need to carefully consider the different frameworks between momentum-domain theory in Fig. 4 and frequency-domain spectroscopy in Fig. 5. Most importantly, the Q-factor is inversely proportional not only to the in-plane damping rate $\gamma = q_{\mathrm{i}}/q_{\mathrm{r}}$ but also to the group velocity v_g of the LPs. In Fig. 5j and k, we plot both quantities for several frequencies as calculated from our complex eigenvalue analysis. From these data, it is clear that the shorter life time of polaritons (corresponding to lower Q-factors) for $|\phi| > 0$ is compensated by the larger group velocity, resulting in a nearly constant propagation length. Thus, a large array of momentum components along the lenticular LP dispersion contributes to enabling directional propagation in real space, as experimentally verified in the following through near-field real-space imaging.

In order to visualize the directional excitation and long-range propagation of LPs in real space, we performed near-field imaging of LPs on a calcite interface with $\theta = 23.3°$. A gold nanodisk (diameter D = 4 μm) was deposited on the interface as an optical antenna that concentrates *p*-polarized mid-infrared illumination (with an oblique incident angle β= 30° along *x*) into a localized hotspot, thus enabling the launching of LPs (as shown in Fig. 6a). The launched field E_{p} propagates along the surface, interfering with the incident field E_{in}, and the interference field is mapped by a sharp metallic tip of scattering-type scanning near-field optical microscope (s-SNOM) with nanoscale resolution. Figure 6a presents the retrieved near-field distribution of disk-launched LPs at $\omega = 883\ \mathrm{cm}^{-1}$, revealing LPs with an arc-type wavefront. The interference between LPs and the incident field renders the momentum of LPs slightly enlarged in k_x by the interference factor $\Delta = k_0 * \cos\varphi$. Figure 6b presents the FT of the near-field distribution in Fig. 6a, confirming the peculiar lenticular shape of IFC and its closed topology in *k*-space. The yellow dashed line indicates the FSLC, and the red solid line presents the theoretical dispersion, exhibiting good agreement between theoretical and experimental results. At frequency $\omega = 887\ \mathrm{cm}^{-1}$ the measured LP fields exhibit higher directionality, consistent with the more pronounced flattening of the IFC shown in Fig. 6d, again agreeing well with our theoretical predictions. The directional propagation of LPs observed here is consistent with our numerical simulations at oblique illumination. Figs. 6(e,f) show (e) the spatial field distribution of LPs and (f) the corresponding IFC at $\omega = 890\ \mathrm{cm}^{-1}$ in the transparent regime, in which the directionality of propagation is further enhanced, now being strongly dominated by the flat parts of the lenticular IFC. Both arrows estimated from simulation in Fig. 6c and 6e are closely aligned with the confined directional fields,

demonstrating how the direction of polariton propagation can be fine-tuned by detuning the illumination frequency.

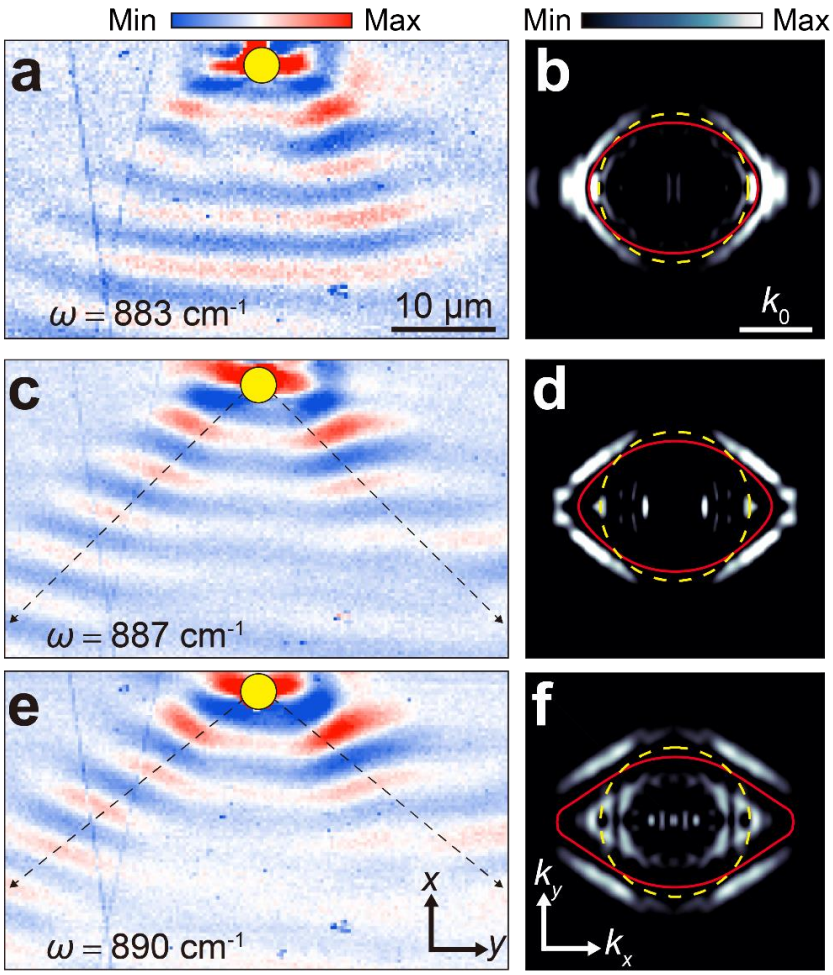

Figure 6. Near-field imaging of directional propagation of LPs in real space. **a**,**c**,**e**. Nanoscale imaging of LPs at $\omega = 883\text{cm}^{-1},\ 887\text{cm}^{-1}, 890\text{cm}^{-1}$, including both type-I hyperbolic and transparent regimes. The indicated directions in b and c are closely aligned with the confined directional fields, where the black arrows are estimated from simulations. **b**,**d**,**f**. Corrected FT of near-field distribution in a,c,e (Note that the dispersions are flipped by 90° clockwise here for clearer presentation). The dispersions are corrected by considering the shift in transverse wave vector k_x caused by oblique incidence. The dashed yellow lines indicate the FSLC, theory dispersion of LPs are marked by solid red lines.

Across these three years, our research project has been able to unveil through theoretical investigations, *k*-space and real-space near-field measurements totally new forms of polaritons, their control through geometrical parameters and symmetry breaking, robust

topological features and largely enhanced light-matter interactions at topological transitions living at the interface of highly anisotropic materials. We anticipate that the newly discovered polaritons, when combined with wavefront engineering, may have important implications to further expand the role of polaritonics in various applications from mid-infrared to far-infrared imaging, bio-sensing, nanobeam guiding on integrated platforms, as well as directional thermal emission.

3. Topological polaritonics in real space

The topological features of polaritons are not limited to the reciprocal space of their IFCs, but can be enabled also in real space. For instance, surface plasmon polaritons (SPPs) have recently been explored to control phase, spin and orbit angular momentum (OAM) as independent degrees of freedom with topological features [21-27]. Based on these principles, plasmonic vortices carrying a topological charge has been explored to enhance the channel capacity of on-chip optical communication networks. Plasmonic OAMs can selectively couple to the spin of light excitation, inducing spin-orbit interactions and spin-controlled plasmonic phenomena, such as unidirectional routing, plasmonic vortex generation and information detection, opening new opportunities for low-energy information processing and computing. During this project, we have worked on extending these explorations to the polaritonic regime in the mid-IR range is exciting on various fronts: (1) we can expect significantly reduced loss compared to their plasmonic counterparts, further enhancing light-matter interactions and bringing them to a regime that can enable nonlinear operations; (2) mid-IR frequencies are of particular interest for on-chip communications and sensing, since several biomolecules have fingerprints in this range; (3) endowing phonon polaritons with these new degrees of freedom unlocks new forms of low-energy information transport and processing. Low-dimensional phonon-polariton nanomaterials offer an ideal playground to enable this vision. The lack of exploration of hyperbolic polaritons in the context of phase and angular momentum control may be associated with the fact that most polaritonic materials support bulk polariton modes, in contrast with plasmon polaritons that travel at interfaces, making more difficult the excitation, observation, and direct access to these phenomena.

During this project, we demonstrated infrared nanoscale hyperbolic phonon polariton topological vortices (HP^2Vs) induced in pristine hBN thin flakes (Fig. 7a), associated with highly reconfigurable topological charges emerging at the HP^2V center. Our system is composed of a gold (Au) disk with Archimedean spiral shape used to launch HP^2 in hBN. We first studied spin-orbit interactions in this system, revealing unprecedented control of HP^2, the precise generation of nanoscale vortices with associated topological charges locked to the excitation spin. Based on scattering-type scanning near-field microscopy (s-SNOM), HP^2Vs were observed in real space, and spin-orbit control and

tunability were accordingly demonstrated. Our results have been revealing new degrees of freedom and enhanced robustness in HP^2 control based on optical spin-orbit interactions and topological charges, ideally suited for super-resolution sensing and imaging, enhanced light-matter interactions, communications and multiplexing, and particle manipulation at mid-IR frequencies.

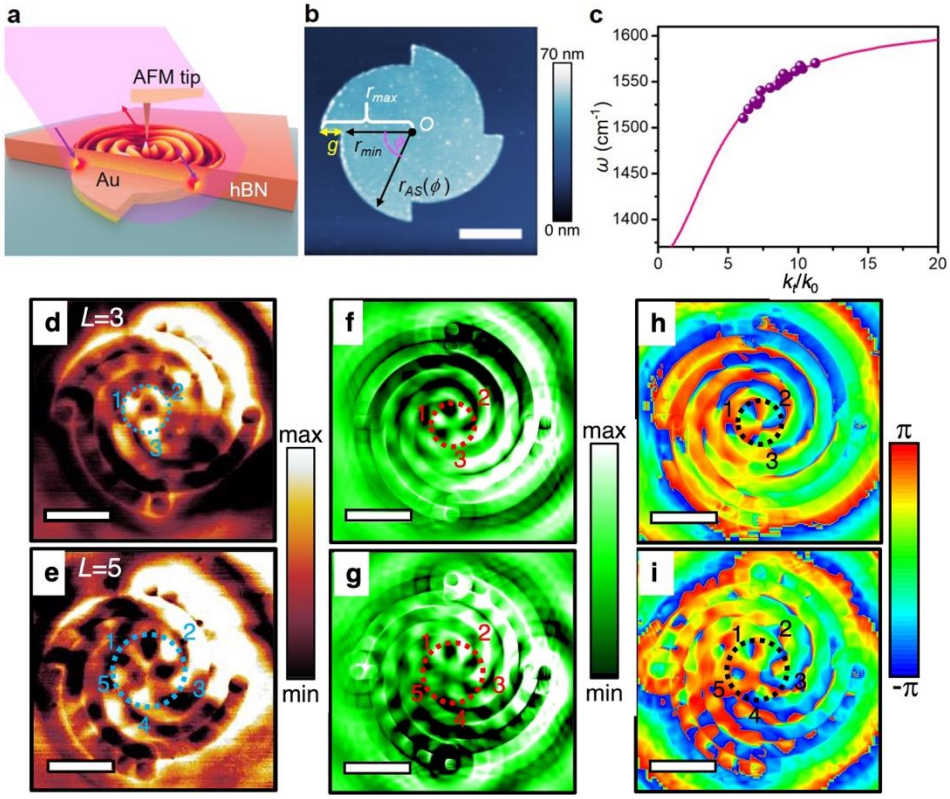

Figure 7. Polariton vortex, dispersion, simulation and experimental results for an hBN flake excited through an Au spiral disk with *m*=4. a, Schematic of the geometry and experimental setup. **b**, AFM image of Au disk shaped as a left-handed Archimedean spiral with four arms, r_{max} and r_{min} are the maximum and minimum radii, g is their difference, ϕ is the azimuthal angle and $r_{AS}(\phi)$ is the distance from the center (O). **c**, Dispersion of k_t for the sample in panel b. Purple spheres and pink curve are experimental and calculated results, respectively. **d-i**, Near-field amplitude images at ~1546 cm^{-1} (**d** and **e**), simulated E_z (**f** and **g**), and phase (**h** and **i**) distributions at ~1546 cm^{-1}. Top and bottom images are obtained under RCP and LCP light illumination, respectively. The black dotted circle in the phase images indicates the spiral phase. The scale bar is 2 μm in all panels.

As schematically illustrated in Fig. 7a, our sample is composed of a thin hBN flake transferred onto a shaped Au disk. The edge of the nanodisk acts as an HP^2 launcher, tailored to convert incident free-space light into strongly confined near fields at the disk

boundary, resulting in efficient launching of HP^{2}s. hBN flakes are known to support discrete waveguide modes based on bulk HP^{2}s, denoted by the mode index *s* associated with their in-plane momentum of $k_{t,s}$, *t* refers to the axis parallel to the hBN flake. Unlike free-space beams or SPPs, HP^2 propagation is characterized by a large wavevector *k* confined to the angle $\theta = \arctan\left(\sqrt{-\frac{\varepsilon_t}{\varepsilon_z}}\right)$ with respect to the optical *z* axis, i.e., the axis perpendicular to the hBN flake. ε_z and ε_t are the hBN permittivity components along the *z* axis and in the orthogonal plane, respectively. Polariton fringes are expected to form with periodicity $\delta_r = 2d\tan\theta$ on the top hBN surface, where *d* is the flake thickness.

In order to generate a polariton vortex in hBN, we control the optical path of the launched hyperbolic polaritons by tailoring the disk shape to follow an Archimedean spiral, $r_{AS}(\phi) = r_{min} + \frac{\mathrm{mod}(m\phi,2\pi)}{2\pi} * g$, where g indicates the rate of increase of the spiral radius with the azimuthal angle ϕ, and the integer parameter *m* denotes the number of spiral arms. As an example, a Au disk with outer shape mapping a four-arm spiral was fabricated, and its atomic force microscope (AFM) image is shown in Fig. 7b, where r_{max} and r_{min} are the maximum and minimum radius and $g \equiv r_{max} - r_{min}$. Based on this design, the polaritons induced on the top surface are expected to support a phase distribution as a function of position (r,ϕ) in the $z = z_0$ plane following

$$\varphi(r,\phi,z_0) = k_{t,s}\left(r_{AS}(\phi) - r_{min} + \frac{\delta_r}{2}\right) + s'2\pi \tag{3}$$

where $s' \equiv s - 1$ is the modified HP^2 order on the flake with a Au substrate. As experimentally verified in Fig. 7, the induced HP^{2}s indeed follow spiral orbitals in space to form a vortex with topological features. In particular, if the Archimedean spiral shape satisfies the condition

$$k_{t,s}\left(g + \frac{\delta_r}{2}\right) = l2\pi, \tag{4}$$

the phase accumulation from $\phi = 0$ to $\phi = 2\pi$ is $m(l + s') * 2\pi$ for an Archimedean spiral with *m* arms. The integer *l* is the orbital topological charge supported by the induced HP^2 spatial distribution.

Under a circularly polarized plane wave excitation, due to spin-orbit interactions in the near-field, the total phase accumulation is $(l * m + \sigma)2\pi$, associated with a topological charge of total angular momentum

$$L = m(l + s') + \sigma\,, \tag{5}$$

where σ = +1 or -1 for left-handed (LCP) or right-handed circularly polarized (RCP) incident light, as we assumed a left-handed spiral. Equation 5 outlines the several degrees

of freedom available to control our HP^{2}Vs, as a result of the complex interplay between incident spin and geometry-induced control of the polariton orbitals. Nontrivial control parameters consist of the spiral geometry (e.g., g), the working frequency (i.e., $k_{t,s}$ and l when g is fixed), the number of spiral arms m, the excited polaritonic mode s', and the excitation spin σ. In our demonstration, we focus on the dominant mode, s'=0.

HP^{2}Vs carrying a discrete topological charge L are expected to support a spiral phase accumulation of L*2π and a phase singularity at their center, controlled by the spin of impinging light. As described by the previous analysis, this spin-dependent phase originates from spin-to-orbital angular momentum conversion enabled by the coupling between the spin angular momentum (SAM) of the excitation and the OAM. To observe HP^{2}Vs and the associated spin-orbit interactions in real space, we used s-SNOM measurements to map HP^{2}s on the top surface of a hBN flake in Fig. 7a. The setup of our experiment is schematically shown in Fig. 8: we fabricated a Au four-arm Archimedean spiral disk over a SiO_2 top layer on a silicon substrate, shown in Fig. 1b, with g = 650 nm, r_{min} = 2.275 μm and height h = 65 nm (details in Methods). Consistent with the previous analysis, the parameter h and r_{min} do not affect the total topological charge induced in the HP^{2}V. An exfoliated hBN flake with a thickness of ~295 nm was transferred on top of the Au disk. By acquiring multiple near-field images with excitation frequency spanning from 1510 cm^{-1} to 1570 cm^{-1}, we retrieved (Fig. 7c) the in-plane momentum (k_t) of the fundamental HP^2 mode at different frequencies.

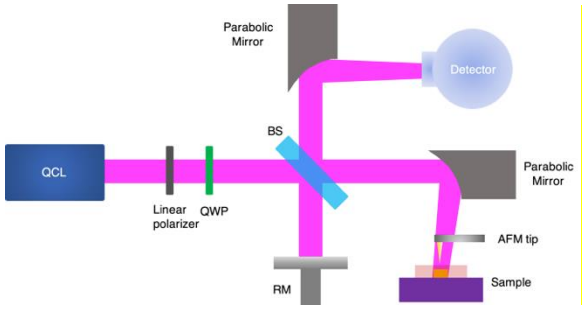

Figure 8. Schematic of the s-SNOM (from neaspec GmbH) setup. QWP, BS, QCL, and RM represent the quarter-wave plate, beam splitter, quantum cascade laser, and reference mirror, respectively.

Fig. 7d and e show the measured near-field distribution of polariton fringes at ~1546 cm^{-1}, yielding a clear spiral shape profile emerging from the interference of HP^2 fields launched by the disk boundary with the incident field at the tip. At this frequency, $\lambda_t \approx 761\,\text{nm} = \lambda_0/8.5$, where λ_t and λ_0 are the in-plane and free-space wavelength, respectively, confirming a deeply subwavelength confinement of the induced HP^{2}V. The simulated electric field ($|E_z|$) profile shown in Fig. 7f and g matches well with

experimental results. Consistent with Eq. 5, when l=1 a left-handed spiral with m=4 yields polariton vortices with topological charge L=3 and L=5 for LCP and RCP excitation, respectively. By comparing Fig. 7d and e (or Fig. 7f and g), we notice a distinct difference in induced field profile at the vortex center, associated with the different topological charge. Both experimental and simulation results reveal that HP^2V with L=3 has a smaller ring-shaped profile at its center than L=5, when l is fixed. This is expected, since its size increases with the spiral phase, consistent with other optical and plasmonic vortex studies. Our setup imprints this dynamic into nanoscale phonon polaritons. It should be mentioned that the regions of the dotted circles in Figs. 7f, h, g, i and below figures are determined by the spiral phase at the center in near-field phase images and their positions are chosen to have a minimum deviation from their center to that of the Au patterns. The calculated phase distributions at ~1546 cm^{-1} under RCP and LCP excitation, shown in Fig. 1h (L=3) and Fig. 1i (L=5), reveal clockwise 3*2π and 5*2π spiral phase variations at the origin, further confirming the nature of spin-orbit interactions for σ = +1 and -1. The discrete topological charge associated with these polariton vortices introduces inherent robustness to geometric perturbations associated with topological features, and new degrees of freedom for polaritonic science and technology.

We have also experimentally demonstrated precise reconfigurability of HP^2Vs, besides the incident spin demonstrated in Fig. 7. According to Eq. 5, both orbit topological charge (l) and the Archimedean spiral geometry (m) control the total induced angular momentum of the polariton vortex. Here, l is controlled by the frequency of impinging light when g and d are fixed, following the polariton dispersion. In Fig. 9, using geometric arguments we predict the phase accumulation φ_{PP} along the azimuthal angle ϕ for m=1, 2, 4 when l=1, 2, revealing a broad range of opportunities in terms of polariton field profiles and induced topological charges that can be generated using this platform. In these plots, we do not explicitly take into account the additional degree of freedom stemming from the excitation spin, which enables an additional knob for manipulation. Because a large L leads to more dramatic amplitude and phase variations, and higher-order HP^2Vs correspond to sharper field profiles, which are more difficult to image, in the following we demonstrate this broad reconfigurability for m=1, 2 and l=1, 2.

We first explored the near-field profile of the induced HP^2Vs and their dependence on the number of Archimedean spiral arms m. Fig. 9b and c show AFM images of Au disks with one- and two-arm Archimedean spirals, i.e., m=1, 2, respectively. The parameters g, r_{min}, and h are the same as in the previous examples, and a thinner exfoliated hBN flake with d ~170 nm was transferred on top of the Au disks. Our experimentally measured polariton dispersion agrees well with the analytical one also for this flake (Fig. 9d), showing larger transverse wavevectors, i.e., more confined polariton fields, compared to the results in Fig. 7c, due to the thinner nature of this flake. As seen in Eq. 4, larger wavevectors

enable access to larger l for fixed g, hence supporting vortices with l=1 and l=2 around 1542 cm^{-1} and 1561 cm^{-1}. Based on Eq. 3, for l=1 we expect L = 0 (1) when m = 1 (2) under RCP light excitation, and L = 2 (3) when m = 1 (2) for LCP light.

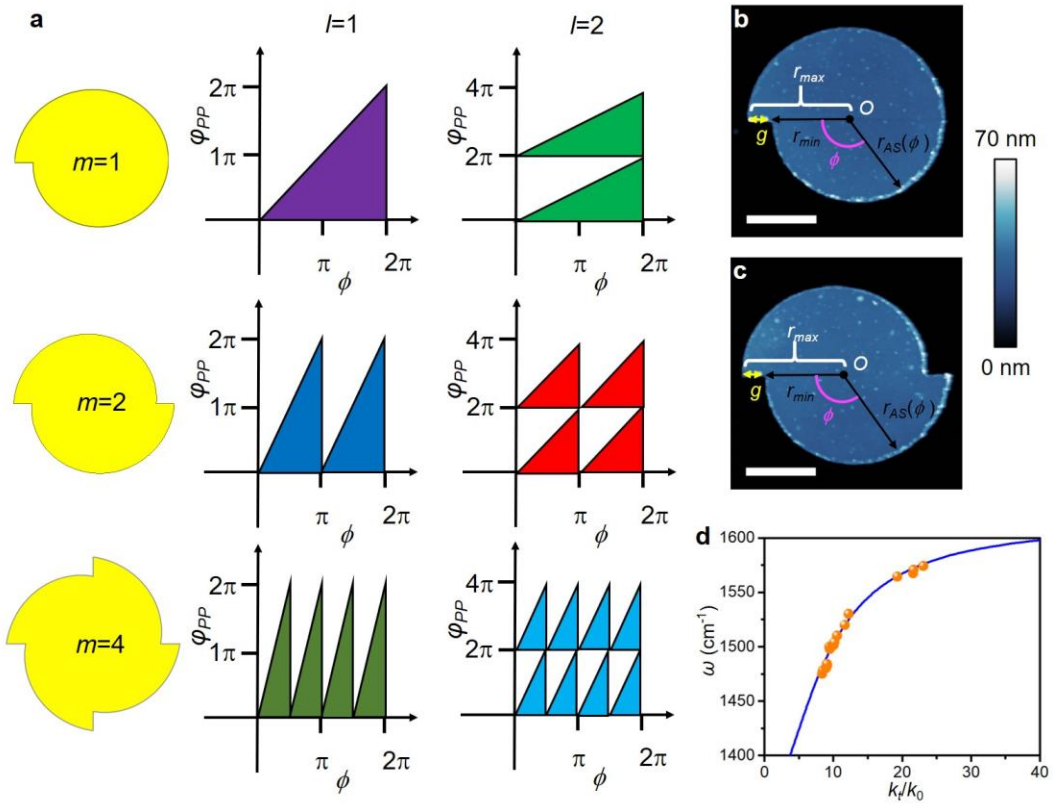

Figure 9. Polariton vortex phase accumulation vs azimuthal angle for *m*=1, 2 and 4 when *l*=1 and 2, and Au disk images and k_t dispersion for polaritonic vortices with *m*=1, 2. a, φ_{PP} and ϕ denote the accumulated phase and azimuthal angle, respectively. **b**,**c**, AFM images of Au disk with one (**b**) and two (**c**) left-handed Archimedean spiral arms. **d**, Dispersion of k_t for samples in panel **b**,**c**. Orange dots and navy curve are experimental and calculated results, respectively.

The corresponding near-field images, showcasing the wide reconfigurability of polariton vortices enabled by these structures, are shown in Fig. 10. For L=0, the phase distribution around the HP^{2}V center is uniform, supporting a subwavelength polariton focal spot, rather than a ring profile as expected for nonzero topological charges (Fig. 10a). Figure 10e shows the corresponding numerical simulations, showing a good agreement. By varying the number of spiral arms or the excitation SAM, we can reconfigure the topological charge L. For example, increasing m from 1 to 2 makes L increase from 0 to 1, resulting in a different size of the central spot, which becomes ring-shaped and grows

larger, as seen comparing Fig. 10a,c (Fig. 10e,g for simulations). Further growth of the central ring profile is obtained under LCP illumination (Fig. 10b and d), as this SAM yields larger values of *L*, again confirmed by our numerical simulations (Fig. 10g and h). It should be noticed that as revealed by the associated spiral phase in Fig. 10f the upper bright lobe close to the central amplitude profile in Fig. 10d is not a part of the central pattern while at an outer layer of the spiral pattern, so *L* is 2 not 3 in Fig. 10b. As *L* increases, we also verify that the polariton vortex phase accumulation grows in discrete 2π steps, as illustrated in Fig. 10i-l. We find 0 to 3*2π spiral phase accumulation around the center, confirming a discrete growth of topological charge *L* from 0 to 3. These images also show a 2*2π phase difference between LCP and RCP excitation, demonstrating strong spin-orbit polariton interactions.

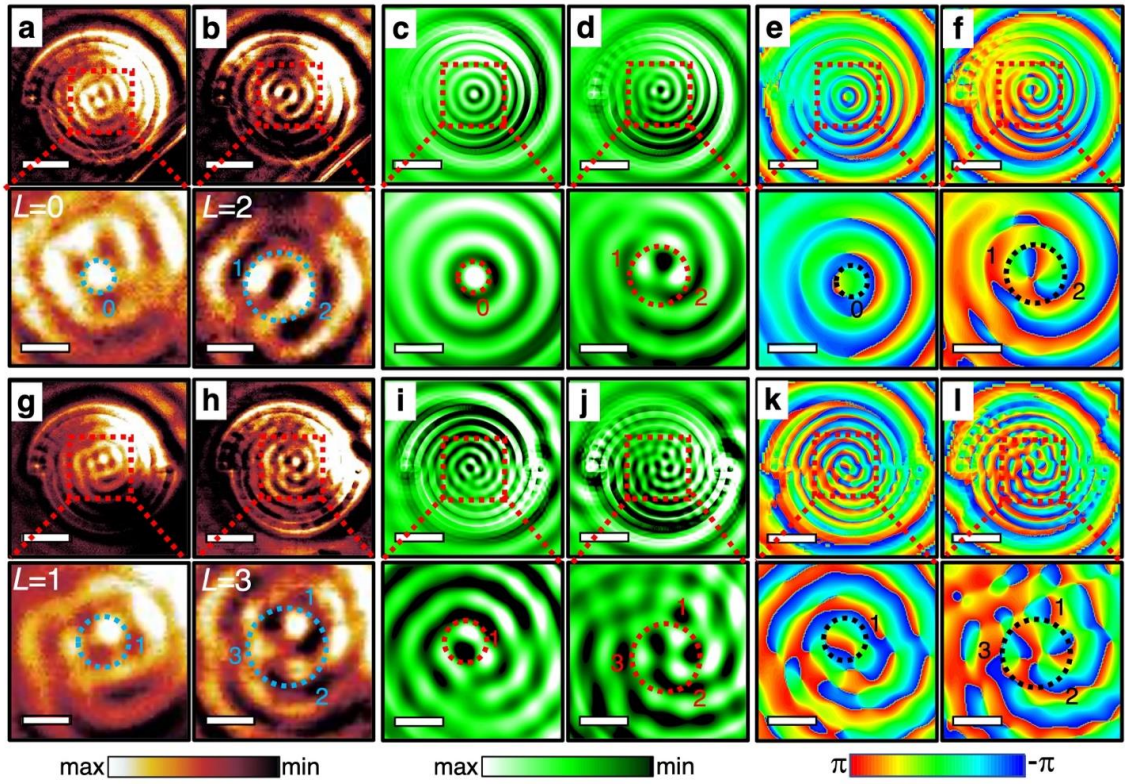

Figure 10. Experimental and simulation results for polariton vortices when *l*=1. a,b,g,h, Near-field amplitude images at ~1550 cm^{-1} for right-handed (**a** and **g**) and left-handed (**b** and **h**) circularly polarized light. **c,d,i,j,** Numerical E_z and **e,f,k,l,** phase distributions at ~1542 cm^{-1} for right-handed (**c**, **i**, **e**, and **k**) and left-handed (**d**, **j**, **f**, and **l**) circularly polarized light. The zoom-in images of the central profile are in the lower column. The cyan/red dotted circles with numbers in the zoom-in amplitude/simulated E_z images label the central interference profiles. The black dotted circles in the phase images with numbers indicate the spiral phases. The scale bars are 2 μm in the full images and 0.67 μm in the zoom-in ones.

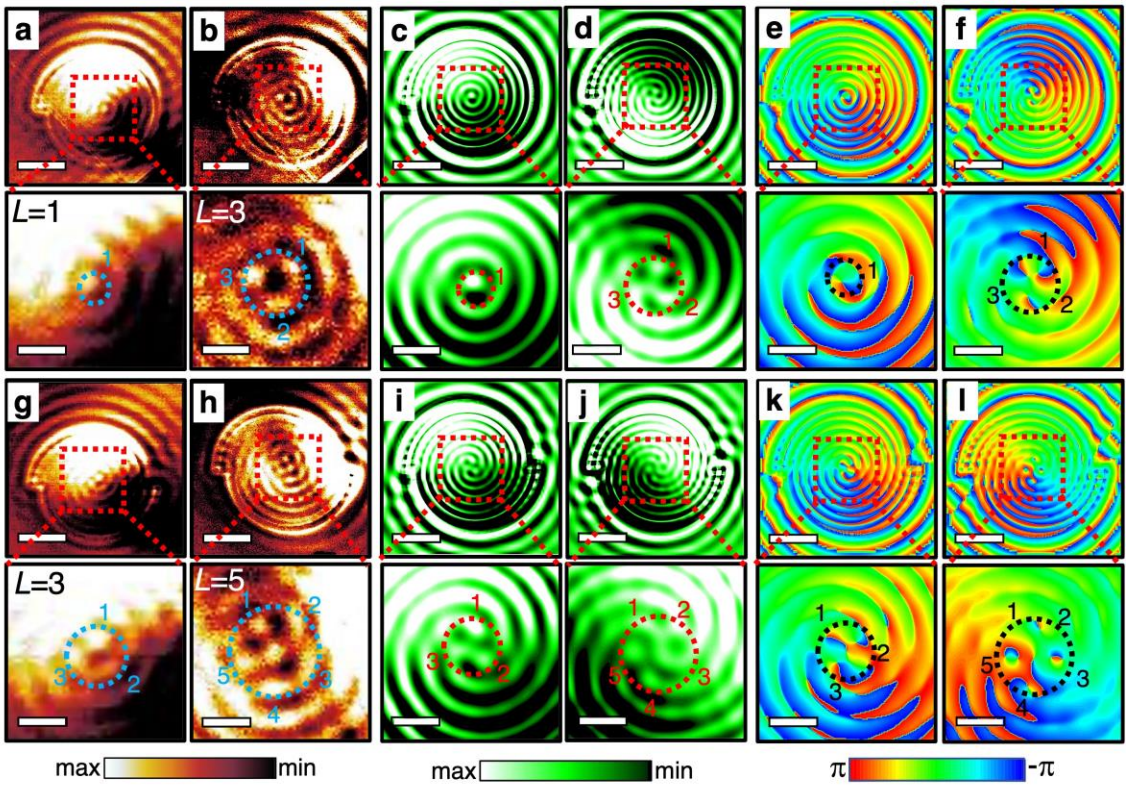

Figure 11. Experimental and simulation results for polariton vortices when *l*=2. a,b,g,h, Near-field amplitude maps at ~1566 cm^{-1} for right-handed (**a** and **g**) and left-handed (**b** and **h**) circularly polarized light. **c,d,i,j,** Numerical E_z, and **e,f,k,l** phase distributions at ~1561 cm^{-1} for right-handed (**c**, **i**, **e**, and **k**) and left-handed (**d**, **j**, **f**, and **l**) circularly polarized light. The zoom-in images of the central profile are in the lower column. The cyan/red dotted circles with numbers in the zoom-in amplitude/simulated E_z images label the central interference profiles. The black dotted circles in the phase images with numbers indicate the spiral phases. The scale bars are 2 μm in the full images and 0.67 μm in the zoom-in ones.

Extreme HP^2V reconfigurability can also be achieved by controlling the orbital topological charge *l*, which can be tuned through the excitation frequency. Figure 11 shows results with a similar trend as in Fig. 10 retrieved from the same samples at ~1561 cm^{-1}, for which the increased k_t of the supported polaritons yields an orbital topological charge *l*=2. As a result, the total angular momentum of HP^2V correspondingly increases compared to the *l*=1 scenario. Since HP^2s support a broad range of frequency-dependent k_t thanks to their hyperbolic dispersion [11,13], a wide range of *l* can be attained, enabling broad reconfigurability of HP^2Vs without varying the sample geometry. The demonstrated nano-vortices have deeply subwavelength spatial profile, again supported

by the extreme HP^2 field confinement. A comparison between experimental and simulated images in Figure 10 and Figure 11 shows that even denser fringes are obtained when l=2, consistent with the larger k_t and shorter polariton wavelength (Eq. 3) combined with increased topological charge. At ~1542 cm^{-1} (Fig. 10a-d), $\lambda_t \approx \lambda_0/14.8$ (l=l), while at ~1567.5 cm^{-1} (Fig. 11a-d) $\lambda_t \approx \lambda_0/19.5$ (l=2). The near-field profiles at the vortex center are supported through the superposition of HP^2s excited from the Au disk boundary, so we can expect that the size of the HP^2V central profile narrows as l increases. To further explore how the phase profile evolves with l, we compare Fig. 10d,h, and l (l=1) with Fig. 11c, g, and k (l=2). A sharper phase variation and a smaller central profile can indeed be observed at the higher frequency, despite the fact that in both scenarios the induced topological charge is the same (L=3). For the L=5 scenario when l=2 in Fig. 11l the spiral phase is less well defined compared to the one in Fig. 1i, associated with the fact that the spiral phase is less stable at larger L when l=2 than l=1. Overall, Figure 11 features HP^2s with very large transverse momentum, realizing polariton vortices with highly confined features, offering unprecedented opportunities for super-resolution mid-IR imaging, high-precision particle manipulation, sensing, and high-density information storage and transmission. When l is larger than 2 the associated frequencies become too close to the 1610 cm^{-1}. Therefore, it is not possible to obtain a clean central profile in this scenario, because of increased loss and reduced group velocity of the associated polaritons.

The demonstrated devices generate broadly reconfigurable topological charges in real space, showcasing exotic polaritonic features, including spin-orbit interactions and nanofocusing. The demonstrated polariton vortices are highly tunable using various degrees of freedom, including the excitation spin, the geometry of the polariton launcher, and the hyperbolic features of the underlying material controlled by the wavelength of excitation. Our demonstration of HP^2V opens unique opportunities to robustly process multiplexed information at mid-IR wavelengths and has great potential for super-resolution imaging systems with multiplexing capabilities, ultracompact mid-IR sensors, and miniaturized polaritonic devices with robust features associated with their topological nature, as well as enhanced nonlinearities and sensing. Overall, our findings broadly enrich the nanophotonic and polaritonic platforms enabled by vdW nanomaterials with phase, spin, and orbital angular momentum engineering capabilities, of great interest for a variety of classical and quantum applications.

4. Topological photonics in synthetic space

Finally, in our work we have been working on topological concepts emerging in the space of the parameters of photonic systems. In particular, we have been particularly interested in demonstrating in compact and accessible systems the nontrivial topological

features of exceptional points and photonic singularities emerging in systems whose parameters obey parity-time symmetry. The exotic physics emerging in non-Hermitian systems with balanced distributions of gain and loss has recently drawn a great deal of attention. These systems exhibit phase transitions and exceptional point singularities in their spectra, at which eigen-values and eigen-modes coalesce and the overall dimensionality is reduced. So far, these principles have been implemented at the expense of precise fabrication and tuning requirements, involving tailored nano-structured devices with controlled optical gain and loss. In this project, on the contrary, anti-parity-time symmetric phase transitions and exceptional point singularities, together with their topological features, have been demonstrated in a single strand of single-mode telecommunication fiber, using a setup consisting of off-the-shelf components and relying on optical nonlinearities. Two propagating signals are amplified and coupled through stimulated Brillouin scattering, enabling exquisite control over the interaction-governing non-Hermitian parameters. As described in the following, singular response to small-scale variations and topological features arising around the exceptional point have been experimentally demonstrated with large precision, enabling robustly enhanced response to changes in Brillouin frequency shift.

In order to demonstrate these features, we have relied on a basic two-level system. Two-level system models are widely studied in several branches of physics, as they can capture a wide range of phenomena in nature. In most scenarios of interest, their dynamics are well characterized by a 2x2 Hermitian Hamiltonian, which entails real eigen-values and a unitary evolution. Non-conserving systems, with loss and/or gain, are instead described by non-Hermitian Hamiltonians, which generally correspond to complex eigen-values. Real eigen-values can arise in such systems if they obey parity-time (PT) symmetry [28], i.e., if loss and gain are suitably balanced in space. As the non-Hermiticity parameter varies, PT-symmetric systems experience a phase transition, after which their eigen-values become complex. This broken phase arises at the exceptional point (EP) of the system, at which the two eigen-values and eigen-modes coalesce into one [29]. The eigen-values around the EP are extremely sensitive to perturbations in the system parameters, hence EP physics has been raising great interest in recent years [30], both from the fundamental research standpoint and in the context of various signal processing and sensing applications [31], with demonstrations in a number of physical platforms to date [32-42]. For the most part, optics-based realizations have made use of integrated nano-photonic devices and nano-structures, typically relying on coupled micro-resonators with careful control over resonance frequencies, gain and loss balance, and coupling strength. Integrated micro- and nano-devices are compact and provide large design freedom, but at the same time fabrication process variations make the EP singularity difficult to reach, and the post-fabrication tuning of these systems is inherently limited. Moreover, nano-fabrication of specialty devices restricts the compatibility and integration of non-Hermitian systems within standard platforms.

In this project, we demonstrated precise control of the dynamics of a non-Hermitian two-level system around its EP, and their topological features, based on optical nonlinearities, through the propagation of light in standard telecommunication single-mode fibres, creating an anti-PT-symmetric system, and taking advantage of the precise control of signal propagation enabled by Brillouin scattering processes. Our degrees of freedom are two continuous probe signals with precise frequency detuning, on the order of 1 MHz. The two tones are amplified or depleted by a pair of continuous counter-propagating pump waves through backward simulated Brillouin scattering (backward SBS), providing careful control of gain and loss along the fiber.

Our platform provides precise control over coupling strength, frequency separation between the probe tones and detuning from the BFS of the fibre, ideally suited for our demonstration of precise tuning of the system parameters around its EP. Quite remarkably, all employed components in our experiments are readily accessible in most optics labs, and no fabrication is necessary. When the frequency detuning between the two tones and pumps' powers are properly adjusted, we are able to observe a phase transition between anti-PT-symmetric and broken-symmetry regimes, passing through an EP, clearly demonstrating coalescence of the eigen-values. Close to the EP singularity, the system shows enhanced spectral response to small-scale variations in the BFS. These changes may be used to resolve extremely small changes in temperature and axial strain in the fibre, up to temperature changes of 0.1 degrees Kelvin or 2 ppm of axial strain in the fibre, since the BFS at telecommunication wavelengths increases by approximately 1 MHz per degree Kelvin or 20 ppm of axial strain. Our fiber platform also provides an exciting opportunity to study the topological features of non-Hermitian systems around EPs as we intentionally detune the frequency separation between the probe tones and the offset between probes and pumps from the BFS. The topology of non-Hermitian degeneracies has drawn significant attention in recent years [43], triggered by the discovery of an asymmetry in the Riemann surfaces around the EP [44-45]. Adiabatic dynamic variations of the system parameters encircling an EP lead to asymmetric energy transfer [46] and mode switching [47]. Similarly, stationary eigen-modes have also been shown to accumulate a geometric phase after encircling an EP [48]. In our system, non-trivial topology arises in the plane spanned by the offset from the BFS and the ratio between coupling and frequency detuning of the two tones. Based on these principles, we have been able to demonstrate significant linewidth squeezing and the emergence of a discontinuity in the eigen-mode spectra as we cross the EP.

The process at the basis of our findings is illustrated in Fig. 12(a). A pair of comparatively strong continuous pump waves is launched into one end of a standard single-mode fibre [point (2) in the figure]. The two tones are of equal power P_P, and they are detuned by a frequency difference $\Delta\nu \sim 1$ MHz, which can be precisely controlled. A pair of continuous optical probe tones is launched into the opposite end of the same fibre

[point (1)]. The probe frequencies are separated by the same frequency difference $\Delta\nu$. The frequency of the upper (lower) pump tone is set to be higher than the one of the upper (lower) probe tone by the BFS ν_B of the fibre [see Fig. 12(b); in the figure, variations around ν_B, relevant for the following discussion, are marked with $\Delta\nu_B$]. This choice leads to strong SBS interactions between pumps and probes, which introduce a controlled coupling between the two probe tones. The probes' power levels are much weaker than the pumps, and the polarization states of all four waves are aligned throughout the fibre, since we consider a total length L shorter than the beat length of residual linear birefringence to maintain polarization alignment.

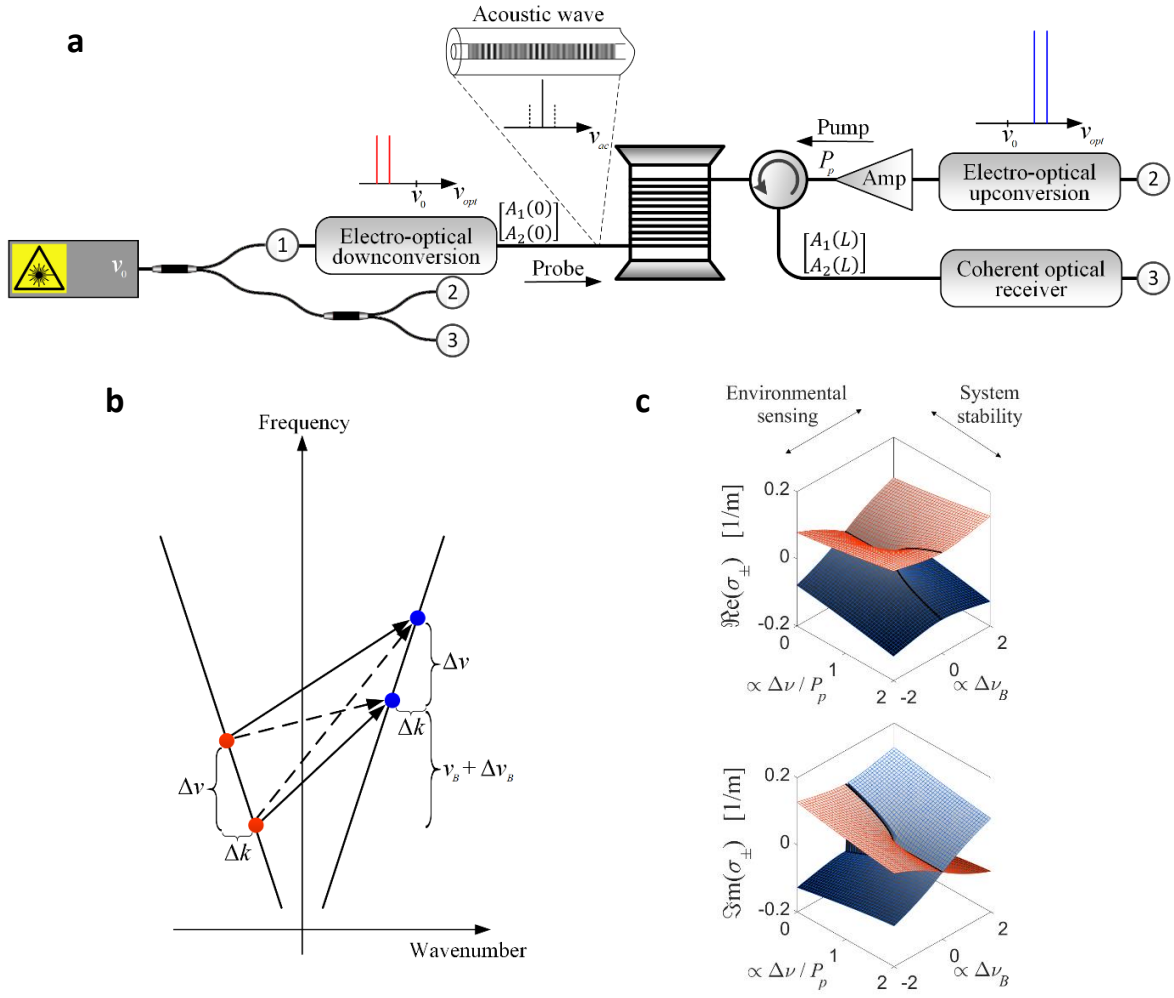

Figure 12. Anti-PT-symmetric Brillouin-enhanced four-wave mixing process. (a) Schematic view of the fibre platform at the basis of our experiments. All optical signals are synthesized from a single, narrow-band laser diode. Electro-optic modulation is used to prepare the input probe states, as well as the SBS pumps. Coherent detection fully

recovers the output probe states. (b) Phase-matching diagram of the participating signals. Both resonant and off-resonant Brillouin interactions (solid and dotted black lines) take place in the fibre. Off-resonance interactions are significant since the detuning $\Delta\nu$ is much smaller than the Brillouin linewidth. (c) Dependence of the probe eigen-values $\sigma_{\pm}$ on the system (ratio between frequency detuning $\Delta\nu$ and SBS pump power P_P) and environmental (manifested through changes in the Brillouin resonance frequency $\Delta\nu_B$) conditions. The bold line refers to a system tuned to the SBS resonance ($\Delta\nu_B = 0$), highlighting the transition from anti-PT-symmetric to a broken-symmetry regime, through the EP (see also experimental results in Fig. 13). Measurements of $\sigma_{\pm}$ as a function of $\Delta\nu_B$ in the vicinity of the EP are shown in Fig. 14 below, and the potential use in Brillouin sensing applications is discussed further in the text.

Backward SBS interactions between pumps and probes generate longitudinal acoustic waves within the fibre at frequencies ν_B, $\nu_B - \Delta\nu$ and $\nu_B + \Delta\nu$. The detuning $\Delta\nu$ is much smaller than the SBS linewidth $\Gamma_B/2\pi$ ~ 30 MHz, hence all three acoustic wave components are significant. The generated acoustic waves mediate the transfer of power from the pump to the probe tones. However, since the SBS gain is only few dB, we may safely assume that the pumps stay undepleted and their power is constant along the entire fiber.

The vector $\vec{A}(z) = [A_1(z), A_2(z)]^T$ contains the complex amplitudes $A_{1,2}$ of the probe tones as a function of position z, and the wavenumber mismatch between the pair of probe tones is $\Delta k = 2\pi n\Delta\nu/c$, where c is the speed of light in vacuum and n is the effective refractive index of the optical mode. The evolution of $\vec{A}(z)$ under steady-state conditions is described by $i\partial\vec{A}/\partial z = \mathcal{H}_0\vec{A}$, with the 2×2 anti-PT-symmetric Hamiltonian:

$$\mathcal{H}_0 \approx \begin{bmatrix} -\left(\Delta k + \frac{\gamma}{2}P_p\Delta\right) + i\gamma P_p & i\frac{\gamma}{2}P_p \\ i\frac{\gamma}{2}P_p & \left(\Delta k + \frac{\gamma}{2}P_p\Delta\right) + i\gamma P_p \end{bmatrix} \equiv \begin{bmatrix} -\widetilde{\Delta k} + ig & ig/2 \\ ig/2 & \widetilde{\Delta k} + ig \end{bmatrix}. \quad (6)$$

Here, γ is the SBS gain coefficient in units of $W^{-1}\times m^{-1}$ and $\Delta \equiv 2(2\pi\cdot\Delta\nu)/\Gamma_B$ is the normalized detuning between probe tones. The Hamiltonian includes SBS amplification of each probe tone $ig \equiv i\gamma P_p$, the coupling between probes $ig/2 \equiv i\frac{\gamma}{2}P_p$, and the total wavenumber mismatch $\widetilde{\Delta k} \equiv \left(\Delta k + \frac{\gamma}{2}P_p\Delta\right)$, which is the sum of Δk and the additional contribution stemming from complex-valued Brillouin gain induced by the two off-resonant acoustic waves. Eq. (6) is valid under the slowly varying envelope approximation and neglects linear losses, which are much smaller than the Brillouin gain in our setup. The Hamiltonian is non-Hermitian and satisfies anti-PT-symmetry, since its diagonal and off-diagonal terms obey the relations $\Im\mathrm{m}(h_{11}) = \Im\mathrm{m}(h_{22})$ and $h_{21} =$

$-h_{12}^{*}$, respectively. The imaginary coupling is due to the joint amplification or depletion of the probes through the acoustic modes, depending on their relative phases. The eigen-values $\sigma_{\pm}$ are the roots of the characteristic polynomial $\det(\mathcal{H}_0 - \sigma I) = 0$, where I is the identity matrix:

$$\sigma_{\pm} = ig \pm \sqrt{\widetilde{\Delta k}^2 - (g/2)^2}. \tag{7}$$

An EP singularity is reached when the wavenumber mismatch equals the coupling strength: $\widetilde{\Delta k} = g/2$. In our system, this requirement is met when pump power and frequency detuning are balanced:

$$\Delta\nu_{EP} = \gamma P_p \Big/ \left[4\pi\left(\frac{n}{c} + \gamma P_p \frac{1}{\Gamma_B}\right)\right]. \tag{8}$$

In Fig. 12(c), we show the real and imaginary parts of the probe eigen-values $\sigma_{\pm}$ as system parameters (ratio between frequency detuning $\Delta\nu$ and SBS pump power P_P) and environmental conditions (manifested through changes in the Brillouin resonance frequency $\Delta\nu_B$) are varied, highlighting interesting topological features arising around the EP. In particular, we observe two interweaving Riemann surfaces centred around the EP and, when the system is tuned to the SBS resonance ($\Delta\nu_B = 0$, bold line in the figure), the eigen-values traverse along the cuts across the Riemann sheets (black curves) as the ratio $\Delta\nu/P_P$ is varied. Adiabatically changing these parameters provides exotic topological features, which we explored and discussed in the following sections.

Figure 13 presents the real and imaginary parts of the two eigen-values $\sigma_{\pm}$ as a function of $\Delta\nu$, with P_P = 27 dBm, comparing their dispersion predicted by Eq. (7) (solid lines) with the retrieved data from measurements (dots). For large values of detuning $\Delta\nu > \Delta\nu_{EP}$, the two eigen-values have the same imaginary part, whereas their real parts differ. As the detuning is reduced, they coalesce at an EP singularity at $\Delta\nu_{EP}$ = 1.145 MHz. Below the EP, the two eigen-values acquire different imaginary parts, manifesting a phase transition and broken symmetry. The measured splitting of the eigen-values agrees very well with our analytical predictions, with discrepancies in the order of 0.001 m^{-1} that may be attributed to various issues: residual imbalance between power levels of the two pump tones, the onset of cascaded SBS processes, small-scale polarization variations affecting the Brillouin gain and coupling strength, and temperature instabilities modifying the BFS. The eigen-values exhibit drastically enhanced sensitivity to variations in $\Delta\nu$ in the EP proximity: the difference between imaginary (real) parts of $\sigma_{\pm}$ scales with $\sqrt{|\Delta\nu - \Delta\nu_{EP}|}$ when $\Delta\nu$ approaches $\Delta\nu_{EP}$ from below (above), in agreement with predictions in other photonic platforms. Further away from the EP, the splitting of eigen-values approaches the linear dependence $|\Delta\nu - \Delta\nu_{EP}|$, as expected. The onset of the EP, the phase transition and square-root-like dispersion around the EP are all

remarkably retrieved in our experiments. Compared to previous experiments in other platforms, the simplicity of our layout and the robust control enabled by SBS processes allow us to resolve the dynamics around the EP with very sharp resolution.

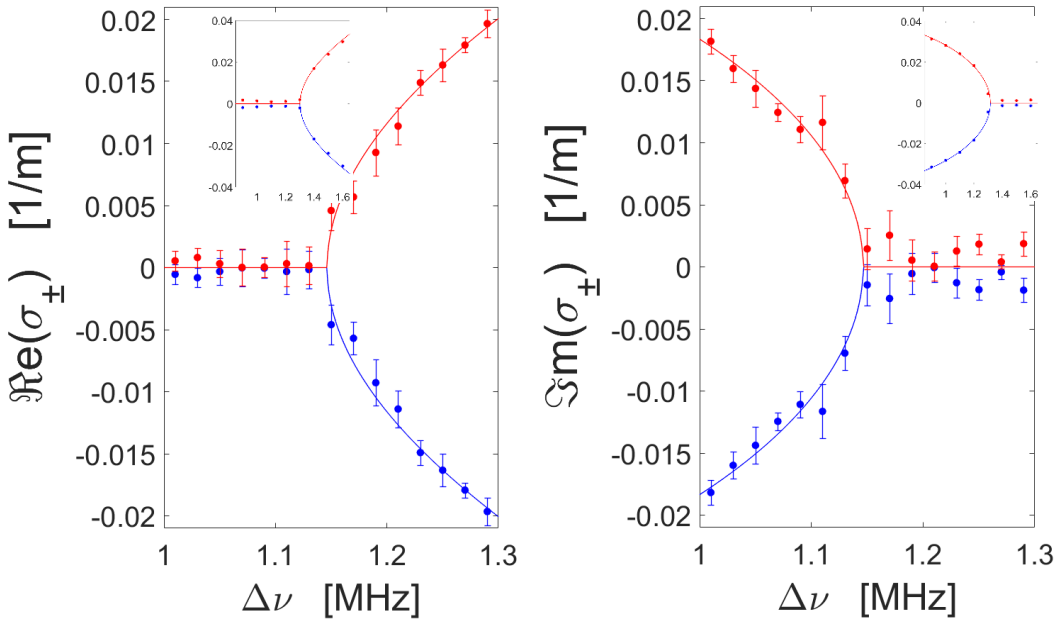

Figure 13. EP singularity and anti-PT-symmetry breaking. Measured (dots) and theoretical (solid lines) $\Re$e (left) and $\Im$m (right) parts of the eigen-values of the system. The means of the two eigen-values have been subtracted. Each point is an average of four measurements and the error bars denote one standard deviation. The phase transition and square-root-like dispersion around the EP is evident. Insets show results over a larger, more coarse scanning range $\Delta\nu$, to highlight the transition towards linear dependence away from the EP.

The enhanced response to perturbations of the system parameters in the vicinity of the EP, as observed in Fig. 13, can also help detect small changes in the BFS ν_B. Consider a frequency offset between the pairs of pump and probe tones that is modified from precisely ν_B to $\nu_B + \Delta\nu_B$ (see also Fig. 13(b)), where $\Delta\nu_B$ is on the order of a few MHz or less. When the normalized detuning is sufficiently small, $\Delta_B \equiv 2(2\pi \cdot \Delta\nu_B)/\Gamma_B \ll 1$, the Hamiltonian of the modified system can be approximated as

$$\mathcal{H} \approx \mathcal{H}_0 + \frac{g}{2}\Delta_B \begin{bmatrix} 2 & 1 \\ 1 & 2 \end{bmatrix}, \tag{9}$$

with eigen-values

$$\sigma_\pm \approx ig + g\Delta_B \pm \sqrt{\widetilde{\Delta k}^2 - (g/2)^2 + ig^2\Delta_B/2}. \tag{5}$$

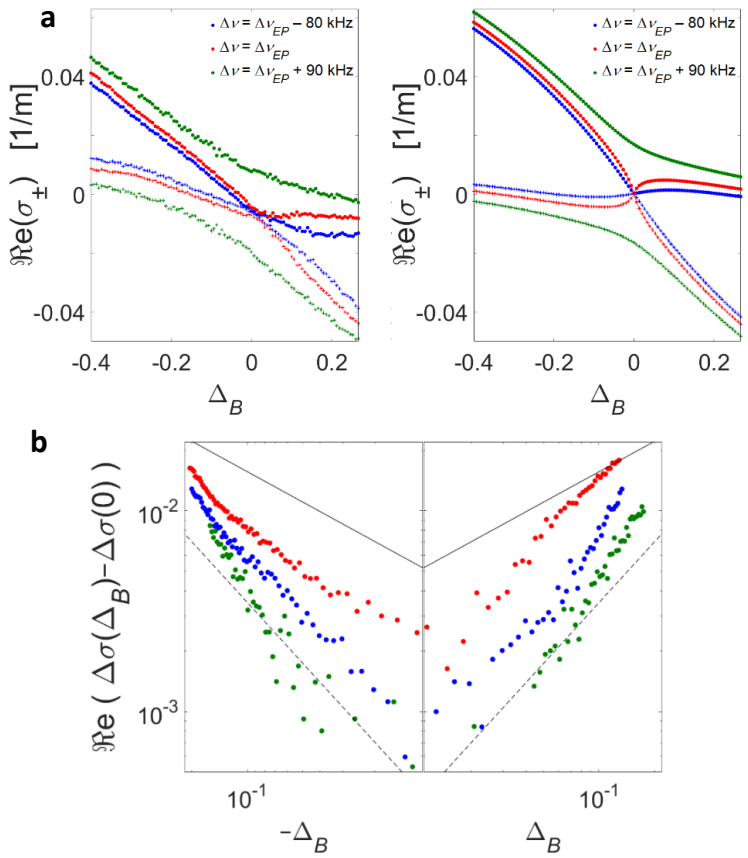

Figure 14. Enhanced sensitivity of the eigen-values to deviations from the BFS at the EP. (a) Measured (left) and calculated (right) $\Re e$ of the eigen-values $\sigma_{\pm}$ as a function of small offsets from the BFS. The frequency detuning between the two probe tones was adjusted above the EP (green, anti-PT-symmetric regime), at the EP (red), or below the EP (blue, broken-symmetry regime), see legends. The real parts of the eigen-values repel each other at the anti-PT-symmetric regime and coalesce at the Brillouin resonance when the symmetry is broken. (b) Measured changes in the splitting of eigen-values as a function of detuning from the BFS: $\Re e[\Delta\sigma(\Delta\nu_B) - \Delta\sigma(0)]$ (logarithmic scale). The colours follow the same legend as in (a). The response is the largest when $\Delta\nu$ approaches $\Delta\nu_{EP}$ (red dots). The logarithmic slope at the EP is smaller than the slopes obtained for $\Delta\nu$ below (blue dots) or above (green dots) the EP. The solid and dotted black lines mark the square root and linear dependence of the splitting on $\Delta_B/2$, respectively.

For small $\Delta_B \neq 0$, the EP singularity cannot be reached using pump waves of equal powers, but when the pump power P_p and probe pair detuning $\Delta\nu$ satisfy the EP condition of the unperturbed system (8), the difference between the two eigen-values is proportional to $\sqrt{\Delta_B}$:

$$\Delta\sigma(\Delta\nu_B) \equiv (\sigma_+ - \sigma_-)/2 \approx \sqrt{i/2}g\sqrt{\Delta_B}. \quad (6)$$

Therefore, the system in the vicinity of its EP is extremely sensitive not only to small changes in $\Delta\nu$, but also to changes in the BFS $\Delta\nu_B$, with similar square-root dependence. The splitting also scales with the Brillouin gain coefficient, in similarity to the SBS gain in uncoupled interactions. Changes to the BFS would be easier to observe in systems with larger Brillouin gain, such as highly nonlinear waveguides. Even greater sensitivity may be obtained with higher-order EPs, arising when considering a larger number of probe tones within the same experimental platform.

Figure 14 shows our observation of enhanced sensitivity to BFS variations in the vicinity of the EP, for a pump power P_P = 28 dBm. The system eigen-values $\sigma_\pm$ were retrieved for different values of $\Delta\nu$ and of the frequency separation between pump and probe pairs, yielding maximum sensitivity for ν_B = 10.7583 GHz ± 50 kHz and probe detuning $\Delta\nu_{EP}$ = 1.31±0.01 MHz. The EP shifts up relative to the value obtained in the experiment of Fig. 2 due to higher pump power used in the current experiment. The residual uncertainty in the estimate of ν_B corresponds to variations in temperature of ±0.05 degrees Kelvin[35]. The uncontrolled laboratory temperature may well have changed over a comparable range during the data acquisition time of about 5 minutes, hence even smaller changes in BFS may be observed in a thermally stable environment. Likewise, a reduction of experimental uncertainty in $\Delta\nu_{EP}$ below 10 kHz would require stabilization of the SBS gain within 0.1%. This condition is difficultly met in the open-loop operation of our platform. The observed precision of BFS measurements shown here therefore represents a lower bound on the attainable sensitivity in better controlled environments.

Figure 14(a) shows measured (left) and calculated (right) real parts of $\sigma_\pm$ as a function of a small offset $\Delta\nu_B$ from the estimated BFS at three different settings of probe pair detuning $\Delta\nu$. In all traces, the minimum separation $\Re\mathrm{e}(\Delta\sigma)$ is observed near $\Delta\nu_B = 0$. In the anti-PT-symmetric regime ($\Delta\nu = \Delta\nu_{EP}$ + 90 kHz, green trace), we observe an avoided crossing for the real parts of the two eigen-values with a nonzero separation even with $\Delta\nu_B = 0$ (see also Fig. 1(c)). In the broken-symmetry regime ($\Delta\nu = \Delta\nu_{EP}$ – 80 kHz, blue trace), and at the EP ($\Delta\nu = \Delta\nu_{EP}$, red trace), the real parts of the two eigen-values do coalesce at $\Delta\nu_B = 0$. The slopes of the eigen-values at the crossing point are higher when the system is at the EP, highlighting the enhanced sensitivity to $\Delta\nu_B$. This property is further illustrated in Fig. 14(b), which shows on a logarithmic scale the effect of $\Delta\nu_B$ on the splitting $\Re\mathrm{e}[\Delta\sigma(\Delta\nu_B) - \Delta\sigma(0)]$. The experimental uncertainty in the eigen-values splitting is in the order of 0.0015 m^{-1}, hence smaller differences can be disregarded. The measured slope of the trace at $\Delta\nu = \Delta\nu_{EP}$ is smaller than the slopes obtained for $\Delta\nu$ below or above the EP, as expected. Enhanced response to small $\Delta\nu_B$ in the EP proximity was also found for the imaginary parts of the eigen-values. However, a complete quantitative description of the imaginary parts of $\sigma_\pm$ on such a fine scale requires that our

model is extended to account for BE-FWM generation of additional probe sidebands, beyond the zero-th order sidebands considered in our analysis.

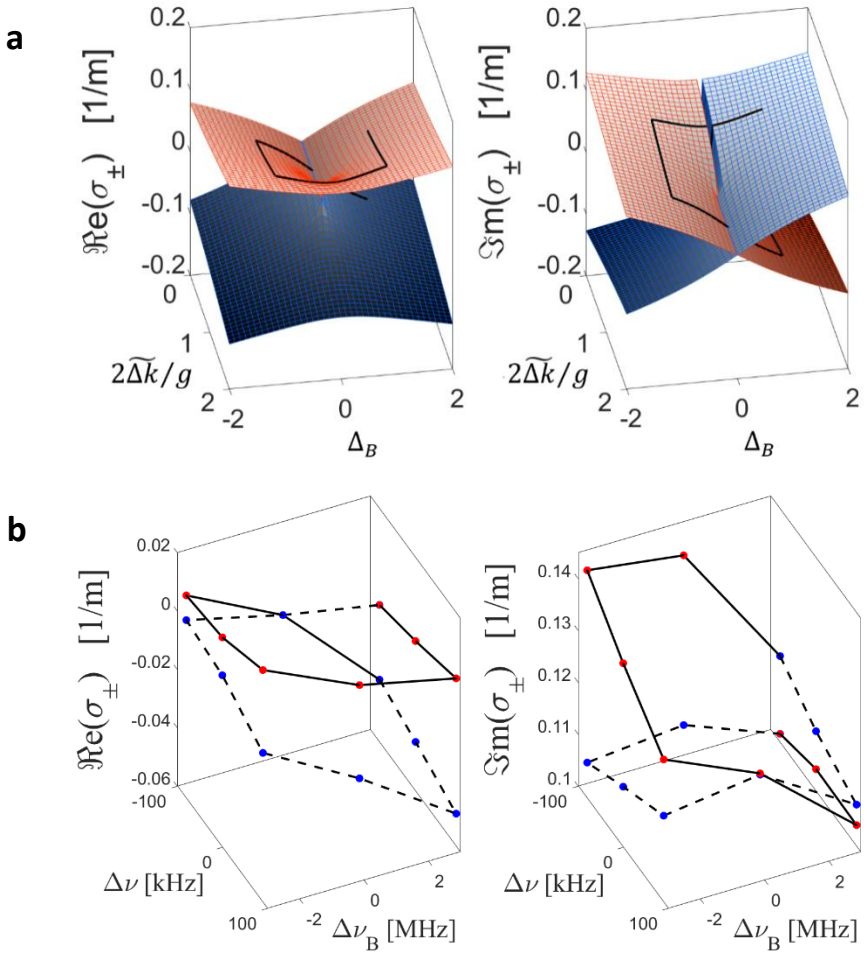

Figure 15. Topological encircling of EP by detuning from the BFS. (a) $\Re$e (left) and $\Im$m (right) parts of the eigen-values of the system σ_+ (red) and σ_- (blue), as a function of the offset Δ_B from the BFS and the ratio between detuning and coupling $2\widetilde{\Delta k}/g$. The means of the two eigen-values have been subtracted for convenience. The solid black line denotes the clockwise trajectory of σ_+, showing the swap with σ_- after one round trip. (b) Traces of real and imaginary parts of the experimentally measured eigen-values as the frequency difference between probes $\Delta\nu$ and offset of the probes from the Brillouin resonance $\Delta\nu_B$ are varied around the EP. The solid and dotted black lines denote the clockwise trajectories of σ_+ and σ_-, respectively. The eigen-values swap after one round trip.

Deviations from the BFS also allow exploring the topological features associated with the EP supported by our platform. Figure 15(a) shows the calculated Riemann sheets of our

Hamiltonian as a function of the relative probe pair detuning $2\widetilde{\Delta k}/g$ and offset Δ_B from the BFS. The surfaces representing the imaginary parts of the two eigen-values intersect each other in the plane Δ_B = 0, whereas the real parts avoid crossing. This difference between real and imaginary parts is introduced by the offset Δ_B. As seen in Eq. (9), the perturbation due to Δ_B introduces real-valued coupling to the modified system Hamiltonian $\mathcal{H}$, whereas the coupling term between the tones in $\mathcal{H}_0$ is purely imaginary. As a result, the real part of the splitting between the roots of $\det(\mathcal{H} - \sigma I) = 0$ [Eq. (10)] is an even function of Δ_B, while the imaginary part is odd. In addition, the imaginary part has a discontinuity at $\{\widetilde{\Delta k} < g/2\,, \Delta_B = 0\}$, but the real parts are equal on this line. Hence, for the eigen-values to continuously change across this line, they have to switch their values (red surface to blue surface). These considerations do not apply for $\{\widetilde{\Delta k} > g/2\,, \Delta_B = 0\}$, so for one turn around the EP in parameter space of Fig. 15(a) we expect one swap of the eigen-values (see the rectangular-spring-shaped black curves in the figure).

This observation is consistent with the topological nature of exceptional points, which manifests itself in the swapping of eigen-modes under an adiabatic encircling of the EP in parameter space. This encircling can be achieved in our system by varying $\Delta\nu$ and $\Delta\nu_B$. From our experimentally recovered eigen-values, we clearly observe this topological feature in Fig. 15(b). As we track the eigen-values around the EP, we are able to experimentally observe the swap. This observation confirms that robust topological modal transfer may be possible in our fibre platform.

Further post-processing of output probe states reveals an additional manifestation of degeneracies in non-Hermitian operators. Enhanced response to small-scale deviations from the BFS may be observed in the eigen-mode projections around the EP. In the anti-PT-symmetric region ($\Delta\nu \gg \Delta\nu_{EP}$), the output projection is Lorentzian with linewidth Γ_B. As we approach and cross the EP, however, the spectral shape changes dramatically. Fig. 16 shows measurements and calculations of the output probe vector $\vec{A}(L)$, projected onto the basis spanned by the eigen-modes of the system. We considered three distinct realizations, with $\Delta\nu = \Delta\nu_{EP}$ + 90 kHz, $\Delta\nu = \Delta\nu_{EP}$ and $\Delta\nu = \Delta\nu_{EP}$ – 80 kHz, as above. In each of them, the detuning Δ_B was scanned within the range ±0.23 ($\Delta\nu_B$ between ±3.5 MHz), and the input probe vector was scanned over N = 18 states of the form $\vec{A}(0) = [1 \quad \exp(j\varphi_m)]^T$, $\varphi_m = 2\pi m/N$, $m = 1 \ldots N$. All input states were chosen with equal magnitudes of the two tones to reduce detrimental effects of residual nonlinearities in the optical modulators. This choice also addresses constructive and destructive interference between the two tones. The figure shows the squared moduli of the two output probe wave components $\left|A_{1,2}(L)\right|^2$ in the eigen-vector basis of $\mathcal{H}(\Delta\nu, \Delta_B)$, as a function of φ_m and Δ_B.

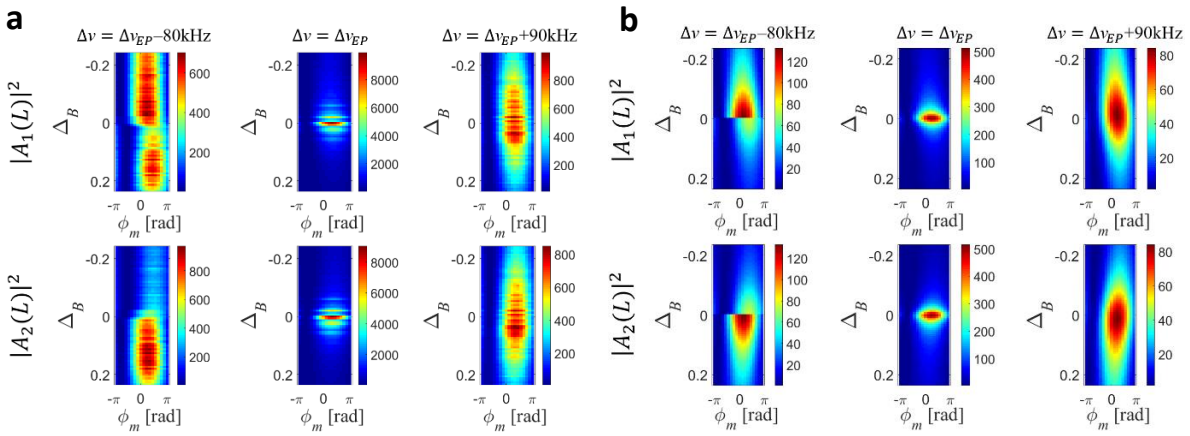

Figure 16. Enhanced response to small-scale variations from the BFS in eigen-mode projections around the EP. (a) Measured and (b) calculated squared moduli of the output probe wave projections as a function of the relative phase φ_m between the input tones and Δ_B, in the eigen-mode basis of $\mathcal{H}(\Delta\nu, \Delta_B)$. The top (bottom) row presents projection on the first (second) eigen-mode. The frequency detuning between the two probe tones $\Delta\nu$ was fixed above the EP (right, anti-PT-symmetric regime), at the EP (centre), or below the EP (left, broken-symmetry regime). The two output projections exhibit significant narrowing when the system approaches the EP from the anti-PT-symmetric regime. Past the EP, asymmetry appears between the two output projections with respect to Δ_B, with discontinuity at the BFS corresponding to a branch-cut in the Riemann sheets.

In the anti-PT-symmetric regime ($\Delta\nu = \Delta\nu_{EP}$ + 90 kHz), the projection amplitudes are enhanced with a linewidth reduced to 4.4 MHz due to the non-orthogonality of the eigen-modes. Unlike the uncoupled case, the projections become strongly dependent on the choice of φ_m and may vary by two orders of magnitude, based on the orientation of the output state with respect to the eigenvectors. When the system operates at the EP (with experimental uncertainty of ±10 kHz as discussed above), the output projections exhibit even more pronounced spectral squeezing, with the enhancement of projection amplitudes narrowing to a Brillouin detuning of 400 kHz. Furthermore, the projections vary by three orders of magnitude among different input phases φ_m. Below the EP ($\Delta\nu = \Delta\nu_{EP}$ – 80 kHz), asymmetry appears between the two output projections with respect to Δ_B, with discontinuity at the BFS. These observations are well supported by the predictions of our model and confirm the EP singularity, providing evidence of a phase transition in the eigen-mode spectra and not only in the spectra of eigen-values. Anyhow, it should be stressed that the narrowing of eigenvector basis shown here may not necessarily lead to dramatic benefits in sensing operations, since the narrowing of the

eigenvector basis makes also the measurement more sensitive to noise, partially offsetting the potential advantages highlighted in Fig. 16.

This result demonstrates the power of nonlinear topological concepts, featuring a non-Hermitian platform in a standard single-mode telecommunication fiber based on the propagation of two continuous probe waves, amplified and coupled through a backward SBS process. The eigen-values of the system depend on the frequency separation between the tones and the SBS pump power. In precisely controlling these two parameters, the system can be brought from an anti-PT-symmetric to a broken-symmetry regime, through an EP. The uncertainty in measurements of the system eigen-values is on the order of 0.001 m^{-1}, ten orders of magnitude smaller than the optical wavenumber. The small uncertainty enables careful observation of the phase transition and the singularities associated with the EP, beyond the limitations of other previously considered platforms for non-Hermitian physics. In particular, our experiments convincingly demonstrate enhanced response to changes in frequency detuning near the EP, and that the response of the eigen-values to changes in the BFS increases near the EP as well.

Our results represent the first realization of non-Hermitian physics, including phase transition and EP singularity, in a single strand of standard optical fibre. Optoelectronic systems employing fibre loops to demonstrate PT-symmetry in coupled fibre ring lasers, optoelectronic oscillators and synthetic dimensions. However, they share many of the characteristics of PT-symmetry and EP studies in integrated devices: their degrees of freedom are optical fields circulating in resonator paths, and precise tuning of resonance frequencies is required. By contrast, the degrees of freedom in our work are co-propagating traveling waves, and no resonances are involved. Moreover, they all make use of external amplifiers to make up for coupling losses, and some use external modulators to establish coupling between the degrees of freedom. Our system on the other hand, employs in-situ traveling-wave amplification and coupling. The accuracy, robustness and flexibility in tailoring the interaction-governing parameters are provided entirely by off-the-shelf components, and they enable the precise observation of the unusual phenomena associated with EPs and non-Hermitian physics in optics.

We have also observed interesting topological features around the EP, in terms of the dependence of the eigen-values on frequency detuning and on deviations from the BFS. The imaginary parts of the eigen-values cross each other when the frequency difference between pumps and probes is scanned through the BFS, whereas the real parts avoid such crossing. These features may enable asymmetric energy transfer, mode-switching and accumulation of geometrical phase, which are now available for study over a basic fiber setup, and in view of recent advances in Brillouin integrated photonics, can be carried over to integrated devices in order to realize configurable wavelength-selective functionalities based on broken symmetries. Overall, our experiments show how the fibre-optics platform may serve as an excellent tool to explore the exotic physics of non-

Hermitian systems, PT-symmetry and EP singularities, leveraging this established platform to access and demonstrate intriguing new phenomena of great interest for basic research and a broad range of applications. Nonlinear wave mixing through SBS also constitutes a suitable playground for studying the interplay between nonlinear parametric gain and PT-symmetry, and the dynamics near EPs in nonlinear non-Hermitian systems.

5. Conclusions

In this report, we have provided an overview of powerful concepts that bring together topological concepts, nanophotonics, enhanced light-matter interactions and nonlinearities, as developed during this project. The outcome of our three-year effort fall within this general theme, but have showcased several other interesting results in this context, encompassing topological light in real, reciprocal and synthetic spaces. The interested reader is referred to the detailed list of publications in the Appendix below.

Appendix

In the following sections, we list the publications produced during our effort, in which more details on our research can be found. We also provide a detailed list of tutorials and seminars given during this three-year effort, conference talks, honors and awards stemming from this research effort, and invention disclosures.

- **Journal papers**

J1. M. A. Miri, and A. Alù, ***"Exceptional Points in Optics and Photonics,"*** Science, Vol. 363, No. 6422, p. 42 (11 pages), January 4, 2019.

J2. Y. Mazor, and A. Alù, ***"Non-Reciprocal Hyperbolic Propagation over Moving Metasurfaces,"*** Physical Review B, Vol. 99, No. 4, 045407 (5 pages), January 8, 2019.

J3. A. Alù, ***"Active and Reconfigurable Metasurfaces,"*** Journal of Optics, in O. Quevedo-Teruel, H. Chen, A. Díaz-Rubio, G. Gok, A. Grbic, G. Minatti, E. Martini, S. Maci, G. V. Eleftheriades, M. Chen, N. I. Zheludev, N. Papasimakis, S. Choudhury, Z. A. Kudyshev, S. Saha, H. Reddy, A. Boltasseva, V. M. Shalaev, A. V. Kildishev, D. Sievenpiper, C. Caloz, A. Alù, Q. He, L. Zhou, G. Valerio, E. Rajo-Iglesias, Z. Sipus, F. Mesa, R. Rodríguez-Berral, F. Medina, V. Asadchy, S. Tretyakov, and C. Craeye, Topical Review, "Roadmap on Metasurfaces," Vol. 21, 073002 (44 pages), July 1, 2019, (***invited paper***).

J4. R. Duggan, J. del Pino, E. Verhagen, and A. Alù, ***"Optomechanically Induced Birefringence and Optomechanically Induced Faraday Effect,"*** Physical Review Letters, Vol. 123, No. 2, 023602 (7 pages), July 9, 2019.

J5. M. A. Miri, M. Cotrufo, and A. Alù, ***"Anomalous Optical Forces in PT-Symmetric Waveguides,"*** Optics Letters, Vol. 44, No. 14, pp. 3558-3561, July 12, 2019.

J6. C. P. Wiederhold, D. L. Sounas, and A. Alù, ***"Nonreciprocal Acoustic Propagation and Leaky-Wave Radiation in a Waveguide with Flow,"*** Journal of the Acoustical Society of America, Special Issue on Non-reciprocal and Topological Wave Phenomena in Acoustics, Vol. 146, No. 1, pp. 802-809, July 31, 2019.

J7. Z. Xiao, Y. Radi, S. Tretyakov, and A. Alù, ***"Microwave Tunneling and Robust Information Transfer Based on Parity-Time-Symmetric Absorber-Emitter Pairs,"*** Research, Vol. 2019, No. 7108494 (10 pages), November 28, 2019.

J8. A. Krasnok, D. Baranov, H. Li, M. A. Miri, F. Monticone, and A. Alù, ***"Anomalies in Light Scattering,"*** Applied Optics and Photonics, Vol. 11, No. 4, pp. 892-951, December 3, 2019, (***invited paper***).

J9. G. D'Aguanno, Y. Hadad, D. A. Smirnova, X, Ni, A. Khanikaev, and A. Alù, ***"Nonlinear Topological Transitions Over a Metasurface,"*** Physical Review B, Vol. 100, No. 21, 214310 (8 pages), December 19, 2019. [PRB Kaleidoscope]

J10. Y. Mazor, and A. Alù, ***"One-Way Hyperbolic Metasurfaces Based on Synthetic Motion,"*** IEEE Transactions on Antennas and Propagation, Special Issue on Recent Advances in Metamaterials and Metasurfaces, Vol. 68, No. 3, pp. 1739-1747, March 1, 2020, (***invited paper***).

J11. A. Krasnok, and A. Alù, ***"Active Nanophotonics,"*** Proceedings of IEEE, Vol. 108, No. 5, pp. 628-654, April 20, 2020, (***invited paper***).

J12. G. Hu, A. Krasnok, Y. Mazor, C. W. Qiu, and A. Alù, ***"Moiré Hyperbolic Metasurfaces,"*** Nano Letters, Vol. 20, No. 5, pp. 3217-3224, May 13, 2020 (published on Apil 16,2020). [Phys.org]

J13. G. Hu, Q. Ou, G. Si, Y. Wu, J. Wu, Z. Dai, A. Krasnok, Y. Mazor, Q. Zhang, Q. Bao, C. W. Qiu, and A. Alù, ***"Topological Polaritons and Photonic Magic Angles in Twisted α-MoO_3 Bilayers,"*** Nature, Vol. 582, pp. 209-213, June 11, 2020. [Physcs World, Phys.org, Independent, many news outlets]

J14. S. Abdollahramezani, O. Hemmatyar, H. Taghinejad, A. Krasnok, Y. Kiarashinejad, M. Zandehshahvar, A. Alù, and A. Adibi, ***"Tunable Nanophotonics Based on Chalcogenide Phase-Change Materials,"*** Nanophotonics, Vol. 9, No. 5, pp. 1189–1241, June 29, 2020, (***invited paper***).

J15. Y. Mazor, and A. Alù, ***"Routing Optical Spin and Pseudospin with Metasurfaces,"*** Physical Review Applied, Vol. 14, No. 1, 014029 (11 pages), July 10, 2020.

J16. A. Ardabi, X. Ni, M. Leamy, and A. Alù, ***"Reconfigurable Floquet Elastodynamic Topological Insulators Based on Synthetic Angular Momentum Bias,"*** Science Advances, Vol. 6, No. 19, eaba8656 (5 pages), July 17, 2020.

J17. P. Li, G. Hu, I. Dolado, M. Tymchenko, C. W. Qiu, F. J. Alfaro-Mozaz, F. Casanova, L. E. Hueso, S. Liu, J. H. Edgar, S. Vélez, A. Alù, and R. Hillenbrand, ***"Collective Near-Field Coupling and Nonlocal Phenomena in Infrared-Phononic Metasurfaces for Nano-Light Canalization,"*** Nature Communications, Vol. 11, No. 3663 (8 pages), July 21, 2020.

J18. R. Duggan, S. A. Mann, and A. Alù, ***"Non-Reciprocal Photonic Topological Order Driven by Uniform Optical Pumping,"*** Physical Review B, Rapid Communications, Vol. 102, No. 10, 100303(R), September 25, 2020.

J19. A. Bergman, R. Duggan, K. Sharma, M. Tur, A. Zadok, and A. Alù, ***"Observation of Anti-Parity-Time-Symmetry, Phase Transitions and Exceptional Points in an Optical Fiber,"*** Nature Communications, Vol. 12, No. 486 (9 pages), January 20, 2021.

J20. A. Overvig, N. Yu, and A. Alù, ***"Chiral Quasi-Bound States in the Continuum,"*** Physical Review Letters, Vol. 126, No. 7, 073001 (6 pages), February 17, 2021.

J21. M. Coppolaro, M. Moccia, G. Castaldi, A. Alù, and V. Galdi, ***"Surface-Wave Propagation on Non-Hermitian Metasurfaces with Extreme Anisotropy,"*** IEEE Transactions on Microwave Theory and Techniques, Special Issue on Metamaterials, Vol. 69, No. 4, pp. 2060-2071, April 1, 2021 (published online on March 2, 2021), (***invited paper***).

J22. G. Hu, C. W. Qiu, and A. Alù, ***"Twistronics for Photons: Opinion,"*** Optical Materials Express, Vol. 11, No. 5, pp. 1377-1382, April 8, 2021, (***invited paper***). [***Editor's Pick***]

J23. G. Hu, M. Wang, Y. Mazor, C. W. Qiu, and A. Alù, ***"Tailoring Light with Layered and Moiré Metasurfaces,"*** Trends in Chemistry, Vol. 3, No. 5, pp. 342-358, May 1, 2021 (published online on March 8, 2021), (***invited paper***). [***Cover***]

J24. S. A. Mann, N. Nookala, S. C. Johnson, M. Cotrufo, A. Mekkawy, J. F. Klem, I. Brener, M. B. Raschke, A. Alù, and M. A. Belkin, ***"Ultrafast Optical Switching and Power Limiting in Intersubband Polaritonic Metasurfaces,"*** Optica, Vol. 8, No. 5, pp. 606-613, April 29, 2021.

J25. X. Ni, S. Kim, and A. Alù, ***"Topological Insulator in Two Synthetic Dimensions Based on an Optomechanical Resonator,"*** Optica, Vol. 8, No. 8, pp. 1024-1032, July 23, 2021.

J26. H. Li, A. Mekawy, and A. Alù, ***"Gain-Free Parity-Time Symmetry for Evanescent Fields,"*** Physical Review Letters, Vol. 127, 014301 (7 pages), July 1, 2021.

J27. A. C. Overvig, S. A. Mann, and A. Alù, ***"Thermal Metasurfaces: Complete Emission Control by Combining Local and Nonlocal Light-Matter Interactions,"*** Physical Review X, Vol. 11, 021050 (29 pages), June 4, 2021. [***APS Physics Focus***, ***Press release, Nature Physics News and Views***]

J28. A. Mekkawy, and A. Alù, ***"Hyperbolic Surface Wave Propagation in Mid-Infrared Metasurfaces with Extreme Anisotropy,"*** Journal of Physics: Photonics, Special Issue 'Focus on Metaphotonics and Metaoptics', Vol. 3, No. 3, 034006 (9 pages), May 28, 2021, (***invited paper***).

J29. G. Hu, C. Zheng, J. Ni, C. W. Qiu, and A. Alù, ***"Enhanced Light-Matter Interactions at Photonic Magic-Angle Topological Transitions,"*** Applied Physics Letters, Special Issue on Twisted 2D Electronic and Photonic Materials and Devices, Vol. 118, 211101 (6 pages), May 24, 2021, (***invited paper***). [***Featured Article***]

J30. A. Vakulenko, S. Kiriushechkina, M. Wang, M. Li, D. Zhirihin, X. Ni, S. Guddala, D. Korobkin, A. Alù, and A. B. Khanikaev, ***"Near-Field Characterization of Higher-Order Topological Photonic States at Optical Frequencies,"*** Advanced Materials, Vol. 33, No. 18, 2004376 (5 pages), May 6, 2021 (published online on March 18, 2021). [***Cover***]

J31. W. Ma, G. Hu, D. Hu, R. Chen, T. Sun, X. Zhang, Q. Dai, Y. Zeng, A. Alù, C. W. Qiu, and P. Li, ***"Ghost Hyperbolic Surface Polaritons in Bulk Anisotropic Crystals,"*** Nature, Vol. 596, pp. 362-366, August 19, 2021. [***Press release***]

J32. M. Li, I. Sinev, F. Benimetskiy, T. Ivanova, E. Khestanova, S. Kiriushechkina, A. Vakulenko, S. Guddala, M. Skolnick, V. Menon, D. Krizhanovskii, A. Alù, A. Samusev, and A. B. Khanikaev, ***"Experimental Observation of Topological Z_2 Exciton-Polaritons in Transition Metal Dichalcogenide Monolayers,"*** Nature Communications, Vol. 12, 4425 (10 pages), July 20, 2021.

J33. S. Guddala, F. Komissarenko, S. Kiriushechkina, A. Vakulenko, M. Li, V. M. Menon, A. Alù, and A. B. Khanikaev, ***"Topological Phonon-Polariton Funneling in Midinfrared Polaritonic Metasurfaces,"*** Science, Vol 374, No. 6564, pp. 225-227, October 8, 2021.

J34. Z. Xiao, and A. Alù, ***"Tailoring Exceptional Points in a Hybrid PT-Symmetric and Anti-PT-Symmetric Scattering System,"*** Nanophotonics, Special Issue in Honor of Mark Stockman, Vol. 10, No. 14, pp. 3723-3733, October 28, 2021 (published online on July 26, 2021), (***invited paper***).

J35. S. Ramezanpour, A. Bogdanov, A. Alù, and Y. Radi, ***"Generalization of Exceptional Point Conditions in Perturbed Coupled Resonators,"*** Physical Review B, Vol. 104, No. 20, 205405 (8 pages), November 3, 2021.

J36. G. Hu, C. W. Qiu, W. Ma, R. Chen, X. Zhang, P. Li, D. Hu, Q. Dai, and A. Alù, ***"Polaritonics on Viking Sunstones,"*** Opics and Photonics News, Special Issue Optics in 2021, Vol. 32, No. 12, p. 49, November 28, 2021. [***Cover***]

J37. A. Krasnok, and A. Alù, ***"Low-Symmetry Nanophotonics,"*** ACS Photonics, Vol. 9, No. 1, pp. 2-24, January 19, 2022 (published online on January 6, 2022), (***invited paper***).

J38. N. C. Passler, X. Ni, G. Hu, J. R. Matson, G. Carini, M. Wolf, M. Schubert, A. Alù, J. D. Caldwell, T. G. Folland, and A. Paarmann, ***"Hyperbolic Shear Polaritons in Low-Symmetry Crystals,"*** Nature, Vol. 602, pp. 599-602, February 23, 2022.

J39. S. Yves, M. I. N. Rosa, Y. Guo, M. Gupta, M. Ruzzene, and A. Alù, ***"Moiré-Driven Topological Transitions and Extreme Anisotropy in Elastic Metasurfaces,"*** Advanced Science, Vol. 9, No. 13, 2200181 (8 pages), May 5, 2022.

- **Book chapters:**

BC1. M. Tymchenko, J. S. Gomez-Diaz, A. Krasnok, M. A. Belkin, and A. Alù, ***"Semiconductor-Loaded Nonlinear Metasurfaces,"*** in Nonlinear Meta-Optics, D. Neshev, F. De Angelis, G. Leo, eds., CRC Press, Taylor & Francis Group, 2020.

- **Invited seminars and tutorials:**

December 19, 2021: "Metamaterials with Broken Symmetry"
Opto-Electronic Forum, Beijing, China (webinar)

December 16, 2021: "Tricking Light and Sound with Metamaterials"
Fall 2021 Doctoral Faculty Meeting, CUNY Graduate Center, New York, NY (webinar)

December 2, 2021: "Exotic Wave-Matter Interactions in Metamaterials with Broken Symmetries"
Physics and Astronomy Colloquium, University of Oklahoma (webinar)

November 9, 2021: "Exotic Wave-Matter Interactions in Metamaterials with Broken Symmetries"
Material Science and Engineering Department Seminar Series, Lehigh University, Bethlehem, PA

October 24, 2021: "Tailoring Light and Sound with Low-Symmetry Metamaterials"
Dan Maydan Prize Ceremony, Ben Gurion University, Israel (webinar)

October 7, 2021: "Metamaterials to Control Light at the Nanoscale"
Master Program in Nanoscience, CUNY Advanced Science Research Center, New York, NY (webinar)

October 4, 2021: "Extreme Wave Phenomena Enabled by Broken Symmetries"
Ginzton Seminar, Stanford University (webinar)

September 28, 2021: "Physical Sciences & Engineering Laureate Presentation"
Blavatnik National Awards Ceremony, New York, NY

September 21, 2021: "Metamaterials"
Four Minutes With, Simons Foundation, New York, NY

September 16, 2021: "Tailoring Wave Phenomena with Broken Symmetries"
European School of Antennas "Exploiting Symmetries in Artificial Materials for Antenna Applications", Paris, France (webinar)

September 13, 2021: "Metamaterial-Based Nanophotonics"
Army Research Office Workshop "Exploring Novel 3D Nano-Assembly Processes for Photonics," Caltech (webinar)

September 2, 2021: "Tailoring Light in Metamaterials with Broken Symmetries"

	Beijing Institute of Technology (webinar)
August 30, 2021:	"Topological Light and Sound" *Summer School on Topological Matter (webinar)*
July 23, 2021:	"Polaritonic Metasurfaces" *METANANO School on Photonics of 2D Materials (webinar)*
July 2, 2021:	"Metamaterial Technologies to Control Light, Radio Waves and Sound" *Lyteloop (webinar)*
June 29, 2021:	"Harnessing Broken Symmetries for Extreme Wave Phenomena" *Langevin summer school 'Wave propagation and control in complex media' (webinar)*
June 2, 2021:	"Polaritonic Metasurfaces" *University of California San Diego (webinar)*
May 13, 2021:	"Dialogues on Metamaterials" *CLEO Workshop (webinar)*
April 28, 2021:	"Metamaterials with Broken Symmetries" *Center for Nanoscale Materials, Argonne National Laboratory (webinar)*
April 15, 2021:	"Exotic Wave-Matter Interactions in Metamaterials" *Distinghuished Lecture, IEEE AP-MTT Bangalore Chapter (webinar)*
Mar. 18, 2021:	"Exotic Interactions with Light and Sound in Metamaterials" *Distinguished Lecture, University of Toronto, Dept. of Electrical Engineering (webinar)*
Mar. 9, 2021:	"Metamaterial Technologies to Control Light, Radio Waves and Sound" *Collins Aerospace (webinar)*
Feb. 26, 2021:	"Exotic Interactions with Light and Sound in Metamaterials with Broken Symmetries" *National Engineers Week, Northeastern University (webinar)*
Feb. 11, 2021:	"Exotic Wave-Matter Interactions Based on Metamaterials" *University of Pavia, Department of Physics (webinar)*
Feb. 4, 2021:	"Optical Metamaterials Based on Broken Symmetries" *New York City College of Technology, Department of Physics (webinar)*
Jan. 19, 2021:	"Metamaterials with Broken Symmetries" *Max Planck Institute of Quantum Optics (webinar)*

Dec. 16, 2020:	"Exotic Wave-Matter Interactions in Metamaterials with Broken Symmetries" *ITMO University (webinar)*
Nov. 17, 2020:	"Optical Metamaterials Based on Broken Symmetries" *Tel Aviv University (webinar)*
Nov. 6, 2020:	"Exotic Wave-Matter Interactions in Metamaterials Based on Broken Symmetries" *University of Illinois at Chicago (webinar)*
Oct. 29, 2020:	"Metamaterials Based on Broken Symmetries" *University of Buffalo (webinar)*
July 29, 2020:	"New Frontiers for Wireless Technology Based on Metamaterials" *Sunway Technologies, Inc. (webinar)*
July 13, 2020:	"Optical Metamaterials Based on Broken Symmetries" *Malaayia NIST (webinar)*
July 9, 2020:	"Mid-Infrared Polaritonic Metamaterials" *Mid-Infrared Discussions (webinar)*
July 1, 2020:	"Photonic Metamaterials Based on Broken Symmetries" *ACS Photonics Global Webinar (webinar, inaugural event)*
June 16, 2020:	"Optical Metamaterials Based on Broken Symmetries" *OSA Metamaterials Technical Group (webinar)*
May 22, 2020:	"Controlling the Flow of Light at the Nanoscale with Broken Symmetries" *New York Academy of Sciences (webinar)*
March 10, 2020:	"New Frontiers for Wave Manipulation Using Metamaterials" *Naval Surface Warfare Center Carderock Division, West Bethesda, MD*
Feb. 26, 2020:	"Exotic Wave-Matter Interactions in Metamaterials with Broken Symmetries" *Kent State University, Kent, OH*
Feb. 13, 2020:	"Exotic Wave-Matter Interactions in Metamaterials with Broken Symmetries" *University of Amsterdam, Amsterdam, Netherlands*
Feb. 7, 2020:	"Metamaterials Based on Broken Symmetries" *University of California Davis, Davis, CA*
Jan. 17, 2020:	"Exotic Wave-Matter Interactions in Metamaterials with Broken Symmetries" *University of Colorado at Boulder, Boulder, CO*

Dec. 3, 2019: "New Frontiers for Wave Manipulation Using Metamaterials"
Hunter College, New York, NY

Dec. 2, 2019: "Metamaterials Based on Broken Symmetries"
University of Chicago, Chicago, IL

Nov. 5, 2019: "Exotic Light-Matter Interactions in Metamaterials"
Rutgers University, New Brunswick, NJ

Oct. 31, 2019: "Excitement about Electromagnetic and Optical Metamaterials"
3M, Minneapolis, MN

Oct. 11, 2019: "Exotic Light-Matter Interactions in Metamaterials"
Courant Institute, New York, NY

Sep. 2, 2019: "New Frontiers for Wave Manipulation Using Metamaterials"
TU Munich, Munich, Germany

July 16, 2019: "Designer Matter: Molding Light and Sound with Meta-Materials"
Blavatnik Science Symposium, New York, NY

July 5, 2019: "Topological and Non-Reciprocal Metamaterials"
TNO, Eindhoven, Netherlands

July 5, 2019: "New Frontiers for Wave Manipulation Using Metamaterials"
TNO, Eindhoven, Netherlands

June 20, 2019: "Designer Matter: Meta-Material Interactions with Light, Radio Waves and Sound"
IEEE AP-S Distinguished Lecture, University Federico II, Napoli, Italy

May 16, 2019: "Designer Matter: Meta-Material Interactions with Light and Sound"
City Tech, Hoboken, NJ

April 26, 2019: "Magnet-Free Non-Reciprocal and Topological Metamaterials"
Brookhaven National Laboratories, Upton, NY

April 25, 2019: "Designer Matter: Meta-Material Interactions with Light, Radio Waves and Sound"
American Physical Society, Ridge, NY

April 22, 2019: "Topological Metamaterials"
Columbia University, New York, NY

- **Conference presentations:**

C1. A. Alù, ***"Polaritonic Metasurfaces,"*** MRS Fall Meeting and Exhibit, November 29-December 8, 2021, (***invited talk***).

C2. M. Wang, G. Hu, and A. Alù, ***"Observation of Hyperbolic Polariton Vortices,"*** MRS Fall Meeting and Exhibit, November 29-December 8, 2021.

C3. A. Alù, ***"Twisted Polaritonics,"*** 43rd PIERS, Hangzhou, China, November 21-25, 2021, (***keynote talk***).

C4. M. Li, I. S. Sinev, F. Benimetskiy, T. Ivanova, E. Khestanova, S. Kiriushechkina, A. Vakulenko, S. Guddala, M. S. Skolnick, V. M. Menon, D. N. Krizhanovskii, A. Alù, A. K. Samusev, A. B. Khanikaev, ***"Observation of Topological Z2 Exciton-polaritons in Transition Metal Dichalcogenide Monolayers,"*** 43rd PIERS, Hangzhou, China, November 21-25, 2021, (***invited paper***).

C5. A. Alù, ***"Polaritonic Metamaterials for Imaging and Sensing,"*** AVS 67th International Symposium and Exhibition, Charlotte, NC, October 24-29, 2021, (***invited talk***).

C6. A. Alù, ***"Polaritonic Metasurfaces,"*** 6th Smart Materials and Surfaces, Milano, Italy, October 20-22, 2021, (***keynote talk***).

C7. A. Alù, ***"Polaritonic Metasurfaces,"*** IEEE Photonics Conference, October 18-21, 2021, (***invited talk***).

C8. A. Alù, ***"Exotic Wave-Matter Interactions in Metamaterials Based on Broken Symmetries,"*** International Conference on Optical and Wireless Technologies (OWT 2021), October 9-10, 2021, (***plenary talk***).

C9. A. Alù, ***"Polaritonic Metasurfaces,"*** Metanano 2021, Tblisi, Georgia, September 13-17, 2021, (***plenary talk***).

C10. A. Alù, ***"Metamaterials Based on Broken Symmetries,"*** XXXIII General Assembly and Scientific Symposium of the International Union of Radio Science (URSI GASS), Roma, Italy, August 29 - September 5, 2021, (***invited talk***).

C11. A. Alù, "***Tailoring Nanoscale Light with Polaritonic Metasurfaces***," AAAFM-UCLA International Conference on Advances in Functional Materials, August 18-20, 2021, (***plenary talk***).

C12. A. Alù, ***"Metamaterials Baked on Broken Symmetries,"*** 2021 IEEE International Conference on Manipulation, Manufacturing and Measurement on the Nanoscale (3M Nano), Xi'an, China, August 2-6, 2021, (***keynote talk***).

C13. A. Alù, ***"Exotic Wave-Matter Interactions in Metamaterials Based on Broken Symmetries,"*** IEEE Research and Applications of Photonics in Defense (RAPID), August 2-4, 2021, (***plenary talk***).

C14. A. Alù, ***"Optical Metamaterials Based on Broken Symmetries,"*** SPIE Optics and Photonics, San Diego, CA, August 1-5, 2021, (***invited talk***).

C15. A. Alù, ***"Polaritonic Metasurfaces,"*** SPIE Photonics West, San Francisco, CA, March 6-11, 2021, (***invited talk***).

C16. N. C. Paßler, T. Folland, J. Matson, X. Ni, G. Hu, M. Wolf, A. Alù, M. Schubert, J. Caldwell, and A. Paarmann, ***"Broken Symmetry of Surface Phonon Polaritons in Monoclinic β-Gallium Oxide,"*** Virtual DPG-Frühjahrstagung (DPG Spring Meeting) of the Surface Science Division, March 1-4, 2021.

C17. A. Alù, ***"Optical Metamaterials Based on Broken Symmetries,"*** Smart Nanomaterials (SNAIA 2020), Paris, France, December 8-11, 2020, (***plenary talk***).

C18. A. Alù, ***"Extreme Wave Interactions in Metamaterials with Broken Symmetries,"*** MRS Fall and Fall Meeting & Exhibit, Boston, MA, November 28-December 4, 2020, (***plenary talk***).

C19. A. Alù, ***"Twisted Polaritonics,"*** MRS Fall and Fall Meeting & Exhibit, Boston, MA, November 28-December 4, 2020, (***keynote talk***).

C20. A. Alù, ***"Exotic Light-Matter Interactions in Metamaterials with Broken Symmetries,"*** MRS Fall and Fall Meeting & Exhibit, Boston, MA, November 28-December 4, 2020, (***tutorial talk***).

C21. A. Alù, ***"Harnessing Broken Symmetries in Metamaterials for Sensing Applications,"*** Istituto Nazional di Ottica (INO)Annual Symposium, Boston, MA, November 28-December 4, 2020, (***keynote talk***).

C22. A. Alù, ***"Exotic Wave-Matter Interactions in Metamaterials Based on Broken Symmetries,"*** International Mechanical Engineering Congress & Exposition (IMECE), Portland, OR, November 15-19, 2020, (***plenary talk***).

C23. A. Alù, ***"Harnessing Broken Symmetries for Extreme Wave Phenomena,"*** Simons MPS Annual Meeting, New York, NY, October 15-16, 2020, (***plenary talk***).

C24. A. Alù, ***"Polaritonic Metasurfaces for Enhanced Light-Matter Interactions,"*** 4th International Conference on Photonics and Optical Engineering (icPOE 2020), Xi'an, China, October 15-16, 2020, (***invited talk***).

C25. M. Barbuto, M.A. Miri, A. Alù, F. Bilotti, and A. Toscano, ***"Topological Phenomena in Antenna Systems,"*** 14th International Congress on Artificial Materials for Novel Wave Phenomena (Metamaterials 2020), New York, NY, September 28 - October 3, 2020.

C26. R. Duggan, S. A. Mann, and A. Alù, ***"Unidirectional Topological Edge Modes in Optically-Driven Dielectric Lattices,"*** 14th International Congress on Artificial Materials for Novel Wave Phenomena (Metamaterials 2020), New York, NY, September 28 - October 3, 2020.

C27. X. Ni, Z. Xiao, A. B. Khanikaev, and A. Alù, ***"A Topolectrical Higher-Order Chern Insulator,"*** 14th International Congress on Artificial Materials for Novel Wave Phenomena (Metamaterials 2020), New York, NY, September 28 - October 3, 2020.

C28. D. Zhirihin, M. Li, M. Gorlach, X. Ni, D. Filonov, A. Slobozhanyuk, A. Alù, and A. B. Khanikaev, ***"Demonstration of High-Order Topological States in Photonic Kagome Lattice with Next-Nearest-Neighbour Coupling,"*** V International Conference on Metamaterials and Nanophotonics (Metanano 2020), Tblisi, Georgia, September 14-18, 2020.

C29. A. Alù, ***"TMD-Based Metasurfaces,"*** SPIE Optics + Photonics, San Diego, CA, August 23-27, 2020, (***invited talk***).

C30. M. Li, D. Zhirihin, M. Gorlach, X. Ni, D. Filonov, A. Slobozhanyuk, A. Alù, A. B. Khanikaev, ***"Photonic Higher-Order Topological States Induced by Long Range Interactions,"*** SPIE Optics + Photonics, San Diego, CA, August 23-27, 2020, (***invited paper***).

C31. A. Vakulenko, S. Kiriushechkina, M. Li, D. Zhirihin, X. Ni, S. Guddala, D. Korobkin, A. Alù, A. B. Khanikaev, ***"Visualization of Topological Transitions and Imaging of Higher-Order Topological States in Photonic Metasurfaces,"*** SPIE Optics + Photonics, San Diego, CA, August 23-27, 2020, (***invited paper***).

C32. A. Alù, ***"Polaritonic Metasurfaces for Extreme Light-Matter Interactions,"*** Gordon Research Conference on Plasmonics and Nanophotonics, Newry, ME, July 12-17, 2020, (***invited talk***).

C33. S. A. Mann, and A. Alù, ***"Broadband Slow Light in Topologically Protected Waveguides,"*** CLEO 2020, San Jose, CA, May 10-15, 2020.

C34. M. Wang, and A. Alù, ***"Nanophotonic Engineering of Monolayer Transition Metal Dichalcogenides,"*** ACS National Meeting & Expo, Philadelphia, PA, March 22-26, 2020, (***invited talk***).

C35. A. Alù, G. Hu, M. Wang, S. Dai, Y. Mazor, A. Krasnok, ***"Hybrid Metasurfaces for Enhanced Light-Matter Interactions and Extreme Polariton Manipulation,"*** Graphene For US, New York, NY, February 20-21, 2020, (***keynote talk***).

C36. A. Alù, ***"TMD-Based Metasurfaces,"*** SPIE Photonics West, San Francisco, CA, February 1-6, 2020, (***invited talk***).

C37. A. Alù, ***"Metamaterials Based on Broken Symmetries,"*** IPAM Workshop on Theory and Computation for 2D Models (TCM 2020), Los Angeles, CA, January 13-17, 2020, (***invited talk***).

C38. A. Alù, ***"Molding Light and Sound with Metamaterials,"*** 27th CAST-USA Annual Convention, New York, NY, October 5, 2019, (***plenary talk***).

C39. D. Zhirihin, M. Li, D. Filonov, X. Ni, A. Slobozhanyuk, A. Alù, and A. Khanikaev, ***"Experimental Observation Of High-order Topological Corner States In 2D Photonic Kagome Lattice,"*** Metamaterials 2019, Roma, Italy, September 16-21, 2019.

C40. S. Mann, A. Mekkawy, and A. Alù, ***"Bounds on Hotspots in Unidirectional Waveguides and Photonic Topological Insulators for Strong, Broadband Light-Matter Interaction,"*** Metamaterials 2019, Roma, Italy, September 16-21, 2019.

C41. A. Alù, ***"New Frontiers for Light Control and Manipulation Using Metamaterials,"*** Nanophotonics and Micro/Nano Optics International Conference (Nanop 2019), Munich, Germany, September 4-6, 2019, (***plenary talk***).

C42. M. Li, X. Ni, M. Weiner, A. Alù, and A. Khanikaev, ***"Topological Phases and Nonreciprocal Edge States in Non-Hermitian Floquet Insulators,"*** SPIE Optics and Photonics 2019, San Diego, August 11-15, 2019.

C43. M. Weiner, X. Ni, M. Li, A. Alù, and A. Khanikaev, ***"Demonstration of a 3rd Order Hierarchy of Topological States in a Three-Dimensional Acoustic Metamaterial,"*** SPIE Optics and Photonics 2019, San Diego, August 11-15, 2019.

C44. A. Alù, ***"Exotic Scattering Features from Metamaterials,"*** Applied Inverse Problems Conference (AIP 2019), Grenoble, France, July 8-12, 2019, (***plenary talk***).

C45. A. Alù***, "Topological and Non-Reciprocal Metamaterials,"*** DIEP Workshop on Topology and Broken Symmetries, Utrecht, Netherlands, July 1-3, 2019, (***invited talk***).

C46. S. Lepeshov, A. Krasnok, and A. Alù, ***"All–Dielectric Nanophotonics with 2D Transition Metal Dichalcogenides,"*** 10th International Conference on Materials for Advanced Technologies (ICMAT 2019), Singapore, June 23-28, 2019.

C47. A. Alù***, "Plasmonic and Polaritonic Metamaterials,"*** Plasmonica 2019, Napoli, Italy, June 19-21, 2019, (***keynote talk***).

C48. A. Alù***, "Magnet-free Non-reciprocity and Topological Order in Electromagnetics,"*** 41st Photonics and Electromagnetics Research Symposium (PIERS 2019), Roma, Italy, June 17-20, 2019, (***invited talk***).

C49. A. Alù, ***"Nonreciprocal and Topological Photonics,"*** CLEO 2019, San Jose, CA, May 5-10, 2019, (***invited talk***).

C50. A. Alù, ***"Topological Metamaterials,"*** APS March Meeting, Boston MA, March 4-8, 2019, (***invited talk***).

C51. N. J. Schilder, S. Peng, X. Ni, J. van de Groep, M. L. Brongersma, A. Alù, A. B. Khanikaev, H. A. Atwater, and A. Polman, ***"Probing the Band Structure of Topological Silicon Photonic Lattices in the Visible,"*** Nanometa, Seefeld, Austria, January 3-6, 2019.

- **Honor and distinctions:**

To the Principal Investigator:

November 16, 2021: 2021 Highly Cited Researcher

Clarivate Analytics Web of Science

Highly Cited Researchers earn this distinction because, during the previous decade, they produced multiple highly cited papers. These are defined as papers ranking in the top 1% by citations, considering both year and field of publication.

June 7, 2021: AAAFM-Heeger Award

American Association for Advances in Functional Materials

'For his seminal contributions to the realization of engineered functional materials and metamaterials, and their applications in electromagnetics, photonics and acoustics'

The AAAFM-Heeger Award (named after Alan J. Heeger, Nobel Laureate) is a prestigious prize conferred on an outstanding, dynamic young researcher for their outstanding achievements and contributions to the field of

Functional Materials. The maximum age considered is 45 years. The awards will be presented at the 3rd AAAFM-UCLA Conference on Functional Materials, which will be held in University California, Los Angeles, June 16-18, 2021.

June 4, 2021: Blavatnik National Award for Young Scientists (Laureate)

The New York Academy of Sciences – Physical Sciences and Engineering Category

The Blavatnik National Awards honor America's most innovative young faculty-rank scientists and engineers. These awards celebrate the past accomplishments and future potential of young faculty members working in three disciplinary categories of science and engineering. The Blavatnik National Awards are conferred at a formal ceremony in New York City each fall. The Laureate receives $250,000, the largest unrestricted scientific prize for America's most innovative young faculty-rank scientists and engineers.

May 12, 2021: Blavatnik National Award for Young Scientists (Finalist)

The New York Academy of Sciences – Physical Sciences and Engineering Category

The Blavatnik National Awards honor America's most innovative young faculty-rank scientists and engineers. These awards celebrate the past accomplishments and future potential of young faculty members working in three disciplinary categories of science and engineering. The Blavatnik National Awards are conferred at a formal ceremony in New York City each fall.

April 7, 2021: Dan Maydan Prize in Nanoscience and Nanotechnology

The Hebrew University of Jerusalem, Center for Nanoscience and Nanotechnology

'For his seminal contributions to nano-optics, nano-photonics, plasmonics and phononics, including the discovery of giant non-reciprocity, non-linear phenomena, and enhanced light-matter interactions using nanostructured materials, metasurfaces and metamaterials'

The $10,000 Dan Maydan Prize in Nanoscience Research is awarded annually to an outstanding mid-career scientist for significant academic achievements in nanoscience and nanotechnology. The prize enables an interchange of knowledge between the Center's scientists and nanoscientists worldwide.

March 16, 2021: Materials Research Society Fellowship

Materials Research Society

'For seminal contributions to the realization of engineered materials and metamaterials, and their several applications in electromagnetics, photonics and acoustics'

The title of MRS Fellow honors those MRS members who are notable for their distinguished research accomplishments and their outstanding contributions to the advancement of materials research, world-wide. The maximum number of new Fellow appointments each year is limited up to

0.2% of the current MRS regular membership and to those with continuous engagement with MRS. Thus, the distinction is highly selective.

Sep. 22, 2020: Breakthrough of the Year in Physics

Physics World

With the paper G. Hu, Q. Ou, G. Si, Y. Wu, J. Wu, Z. Dai, A. Krasnok, Y. Mazor, Q. Zhang, Q. Bao, C. W. Qiu, and A. Alù, "Topological Polaritons and Photonic Magic Angles in Twisted α-MoO3 Bilayers," Nature, Vol. 582, pp. 209-213, June 11, 2020.

Sep. 22, 2020: 2020 Highly Cited Researcher

Clarivate Analytics Web of Science

Highly Cited Researchers earn this distinction because, during the previous decade, they produced multiple highly cited papers. These are defined as papers ranking in the top 1% by citations, considering both year and field of publication.

June 23, 2020: Simons Collaboration on Extreme Wave Phenomena Based on Symmetries

Simons Foundation

Simons Collaborations bring together groups of outstanding scientists to address topics of fundamental scientific importance in which a significant new development has created a novel area for exploration in an established field. They provide up to 16M$ of funding for up to 8 years of basic research activities.

April 27, 2020: Blavatnik National Award for Young Scientists (Finalist)

The New York Academy of Sciences – Physical Sciences and Engineering Category

The Blavatnik National Awards honor America's most innovative young faculty-rank scientists and engineers. These awards celebrate the past accomplishments and future potential of young faculty members working in three disciplinary categories of science and engineering. The Blavatnik National Awards are conferred at a formal ceremony in New York City each fall.

Nov. 26, 2019: National Academy of Inventors Fellowship

National Academy of Inventors

'For having demonstrated a highly prolific spirit of innovation in creating or facilitating outstanding inventions that have made a tangible impact on the quality of life, economic development, and welfare of society'

Election to NAI Fellow status is the highest professional distinction accorded solely to academic inventors. The program has 1,060 Fellows worldwide representing more than 250 prestigious universities and governmental and non-profit research institutes. Collectively, the Fellows hold more than 38,000 issued U.S. patents, which have generated over 11,000 licensed technologies and companies, and created more than 36 million jobs. In addition, over $1.6 trillion in revenue has been generated based on NAI Fellow discoveries. With the induction of the 2018 class, there are now more than 125 presidents and senior leaders of research

universities and non-profit research institutes, 502 members of the National Academies of Sciences, Engineering, and Medicine; 40 inductees of the National Inventors Hall of Fame, 57 recipients of the U.S. National Medal of Technology and Innovation and U.S. National Medal of Science, 34 Nobel Laureates, 3 Queen Elizabeth Prize for Engineering recipients, 304 AAAS Fellows, 200 IEEE Fellows, and 164 Fellows of the American Academy of Arts & Sciences, among other awards and distinctions.

Oct. 25, 2019: AAAS Fellowship

American Association for the Advancement of Science

'For distinguished contributions to the field of electromagnetics and photonics, particularly for the modeling and applications of artificial materials and metamaterials'

AAAS member whose efforts on behalf of the advancement of science or its applications are scientifically or socially distinguished may, by virtue of such meritorious contribution, be elected a Fellow by the Council.

Sep. 15, 2019: 2019 Highly Cited Researcher

Clarivate Analytics Web of Science

Highly Cited Researchers earn this distinction because, during the previous decade, they produced multiple highly cited papers. These are defined as papers ranking in the top 1% by citations, considering both year and field of publication.

June 24, 2019: IEEE Kiyo Tomiyasu Award

IEEE Geoscience and Remote Sensing Society, IEEE Microwave Theory and Techniques Society

'For contributions to novel electromagnetic materials and their application'

The IEEE Kiyo Tomiyasu Award was established in 2001 to recognize outstanding early to mid-career contributions to technologies holding the promise of innovative applications. Recipient selection is administered through the Technical Field Awards Council of the IEEE Awards Board. The award consists of a bronze medal, certificate, and a 10k$ honorarium.

June 21, 2019: IET A F Harvey Prize Engineering Research Prize (Finalist)

Institute of Engineering and Technology

The prize is awarded annually in recognition of an outstanding achievement in engineering research in the fields of medical, microwave and radar or laser/optoelectronic engineering, with the prize fund (350k GBP) awarded to support further research led by the recipient.

May 7, 2019: Blavatnik National Award for Young Scientists (Finalist)

The New York Academy of Sciences – Physical Sciences and Engineering Category

The Blavatnik National Awards honor America's most innovative young faculty-rank scientists and engineers. These awards celebrate the past accomplishments and future potential of young faculty members working in three disciplinary categories of science and engineering. The Blavatnik National Awards are conferred at a formal ceremony in New York City each fall.

May 1, 2019: Vannevar Bush Faculty Fellowship
Department of Defense
The Vannevar Bush Faculty Fellowship (VBFF) is the Department of Defense's most prestigious single-investigator award and supports basic research with the potential for transformative impact. As a 5-year fellowship with up to $3 million in funding, the VBFF supports new, out-of-the box ideas where researcher creativity intersects with the unknown. Vannevar Bush Fellows represent a cadre of experts that provide invaluable direction to the DoD in its scientific efforts and also train the next generation of scientists and engineers.

April 8, 2019: Metamorphose President
Virtual Institute for Artificial Electromagnetic Materials and Metamaterials

To the Involved Students:

October 9, 2020: Guangwei Hu, ***2020 Rising Stars of Light (Finalist),*** Light: Science & Applications

August 7, 2020: Curtis Rasmussen, ***Engineering Fellowship Award,*** The University of Texas at Austin, Austin, TX

August 13, 2019: Sander Mann, ***CUNY Postdoctoral Travel Award,*** City University of New York

References

[1] Dai, S., et al. Tunable phonon polaritons in atomically thin van der Waals crystals of boron nitride. Science 343, 1125-1129 (2014).
[2] Caldwell, J. D. et al. Sub-diffractional volume-confined polaritons in the natural hyperbolic material hexagonal boron nitride. Nat. Commun. 5, 5221 (2014).
[3] Yoxall, E. et al. Direct observation of ultraslow hyperbolic polariton propagation with negative phase velocity. Nat. Photon. 9, 674–678 (2015).
[4] Li, P., et al. Hyperbolic phonon-polaritons in boron nitride for near-field optical imaging and focusing. Nature Commun. 6, 7507 (2015).
[5] Hu, G., Shen, J., Qiu, C.-W., Alù, A., & Dai, S. Phonon Polaritons and Hyperbolic Response in van der Waals Materials. Adv. Opt. Mat. 190193 (2019).
[6] Ma, W. et al. In-plane anisotropic and ultra-low-loss polaritons in a natural van der Waals crystal. Nature 562, 557-562 (2018).
[7] Zheng, Z. et al. Highly confined and tunable hyperbolic phonon polaritons in van der Waals semiconducting transition metal oxides. Adv. Mater. 30, 1705318 (2018).
[8] Zheng, Z. et al. A mid-infrared biaxial hyperbolic van der Waals crystal. Sci. Adv. 5, 5 (2019).
[9] Gomez-Diaz, J. S., Tymchenko, M. & Alù, A. Hyperbolic plasmons and topological transitions over uniaxial metasurfaces. Phys. Rev. Let. 114, 233901 (2015).

[10] Correas-Serrano, D., Gomez-Diaz, J.S., Melcon, A.A. & Alù, A. Black phosphorus plasmonics: anisotropic elliptical propagation and nonlocality-induced canalization. Journal of Optics 18, 104006 (2016).
[11] Gomez-Diaz, J. S. & Alù, A. Flatland optics with hyperbolic metasurfaces. ACS Photonics 3, 2211-2224 (2016).
[12] High, A. A. et al. Visible-frequency hyperbolic metasurface. Nature 522, 192-196 (2015).
[13] L. Sun, C. Y. Wang, A. Krasnok, J. Choi, J. Shi, J. S. Gomez-Diaz, A. Zepeda, S. Gwo, C. K. Shih, A. Alù, and X. Li, Separation of Valley Excitons in a MoS2 Monolayer Using a Subwavelength Asymmewtric Groove Array, Nature Photonics 13, 180 (2019)
[14] Li, P. et al. Infrared hyperbolic metasurface based on nanostructured van der Waals materials. Science 359, 892-896 (2018).
[15] P. Li, G. Hu, I. Dolado, M. Tymchenko, C. W. Qiu, F. J. Alfaro-Mozaz, F. Casanova, L. E. Hueso, S. Liu, J. H. Edgar, S. Vélez, A. Alù, and R. Hillenbrand, Collective Near-Field Coupling and Nonlocal Phenomena in Infrared-Phononic Metasurfaces for Nano-Light Canalization, Nature Communications 11, 3663 (2020).
[16] G. Hu, A. Krasnok, Y. Mazor, C. W. Qiu, and A. Alù, Moiré Hyperbolic Metasurfaces, Nano Letters 20, 3217 (2020).
[17] Cao, Y. et al. Unconventional superconductivity in magic-angle graphene superlattices. Nature 556, 43–50 (2018).
[18] G. Hu, Q. Ou, G. Si, Y. Wu, J. Wu, Z. Dai, A. Krasnok, Y. Mazor, Q. Zhang, Q. Bao, C. W. Qiu, and A. Alù, Topological Polaritons and Photonic Magic Angles in Twisted α-MoO3 Bilayers, Nature 582, 209 (2020).
[19] Ma, W. L. et al. Ghost hyperbolic surface polaritons in bulk anisotropic crystals. Nature 596, 362–366 (2021).
[20] Passler, N. et al. Hyperbolic Shear Polaritons in Low-Symmetry Crystals. Nature 602, 595–600 (2022).
[21] H. Kim, J. Park, S. W. Cho, S. Y. Lee, M. Kang, B. Lee, Synthesis and dynamic switching of surface plasmon vortices with plasmonic vortex lens, Nano Lett. 10, 529–536 (2010).
[22] Y. Yang, L. Wu, Y. Liu, D. Xie, Z. Jin, J. Li, G. Hu, aC. W. Qiu, Deuterogenic Plasmonic Vortices, Nano Lett. 20, 6774–6779 (2020).
[23] S.-W. Cho, J. Park, S.-Y. Lee, H. Kim, B. Lee, Coupling of spin and angular momentum of light in plasmonic vortex, Opt. Express 20, 10083 (2012).
[24] A. David, B. Gjonaj, G. Bartal, Two-dimensional optical nanovortices at visible light, Phys. Rev. B 93, 1–5 (2016).
[25] G. Spektor, A. David, G. Bartal, M. Orenstein, A. Hayat, Spin-patterned plasmonics: towards optical access to topological-insulator surface states, Opt. Express 23, 32759 (2015).
[26] C. Khandekar, Z. Jacob, Thermal spin photonics in the near-field of nonreciprocal media, New J. Phys. 21, (2019).
[27] Z. Jin, D. Janoschka, J. Deng, L. Ge, P. Dreher, B. Frank, G. Hu, J. Ni, Y. Yang, J. Li, C. Yu, D. Lei, G. Li, S. Xiao, S. Mei, H. Giessen, F. M. zu Heringdorf, C.-W. Qiu, Phyllotaxis-inspired nanosieves with multiplexed orbital angular momentum, ELight 1, 1–11 (2021).

[28] Bender, C. M. & Boettcher, S. Real spectra in non-hermitian hamiltonians having PT symmetry. Phys. Rev. Lett. 80, 5243–5246 (1998).
[29] Heiss, W. D. Exceptional points of non-Hermitian operators. J. Phys. A. Math. Gen. 37, 2455 (2004).
[30] Christodoulides, D. & Yang, J. Parity-time Symmetry and its Applications. vol. 280 (Springer, 2018).
[31] El-Ganainy, R. et al. Non-Hermitian physics and PT symmetry. Nat. Phys. 14, 11–19 (2018).
[32] Benisty, H. et al. Implementation of PT symmetric devices using plasmonics: principle and applications. Opt. Express 19, 18004 (2011).
[33] Regensburger, A. et al. Parity-time synthetic photonic lattices. Nature 488, 167–171 (2012).
[34] Miri, M. A. & Alù, A. Exceptional points in optics and photonics. Science (80-.). 363, (2019).
[35] Zhang, Z. et al. Observation of Parity-Time Symmetry in Optically Induced Atomic Lattices. Phys. Rev. Lett. 117, 1–5 (2016).
[36] Peng, P. et al. Anti-parity-time symmetry with flying atoms. Nat. Phys. 12, 1139–1145 (2016).
[37] Jiang, Y. et al. Anti-Parity-Time Symmetric Optical Four-Wave Mixing in Cold Atoms. Phys. Rev. Lett. 123, 1–6 (2019).
[38] Zhang, X., Ding, K., Zhou, X., Xu, J. & Jin, D. Experimental Observation of an Exceptional Surface in Synthetic Dimensions with Magnon Polaritons. Phys. Rev. Lett. 123, 237202 (2019).
[39] Sakhdari, M. et al. Experimental Observation of PT Symmetry Breaking near Divergent Exceptional Points. Phys. Rev. Lett. 123, 193901 (2019).
[40] Shi, C. et al. Accessing the exceptional points of parity-time symmetric acoustics. Nat. Commun. 7, 1–5 (2016).
[41] Lustig, B., Elbaz, G., Muhafra, A. & Shmuel, G. Anomalous energy transport in laminates with exceptional points. J. Mech. Phys. Solids 133, 103719 (2019).
[42] Özdemir, K., Rotter, S., Nori, F. & Yang, L. Parity–time symmetry and exceptional points in photonics. Nat. Mater. 18, 783–798 (2019).
[43] Gong, Z. et al. Topological Phases of Non-Hermitian Systems. Phys. Rev. X 8, 31079 (2018).
[44] Dembowski, C. et al. Experimental observation of the topological structure of exceptional points. Phys. Rev. Lett. 86, 787–790 (2001).
[45] Dembowski, C. et al. Encircling an exceptional point. Phys. Rev. E - Stat. Physics, Plasmas, Fluids, Relat. Interdiscip. Top. 69, 7 (2004).
[46] Xu, H., Mason, D., Jiang, L. & Harris, J. G. E. Topological energy transfer in an optomechanical system with exceptional points. Nature 537, 80–83 (2016).
[47] Doppler, J. et al. Dynamically encircling an exceptional point for asymmetric mode switching. Nature 537, 76–79 (2016).
[48] Gao, T. et al. Observation of non-Hermitian degeneracies in a chaotic exciton-polariton billiard. Nature 526, 554–558 (2015).